Doctoral Dissertations

Student Theses and Dissertations

Fall 2019

Accurate monitoring of x, y, and z magnetization for analysis of hardware and pulse sequence performance in NMR spectroscopy

Emmalou Theresa Schmittzehe

Recommended Citation

ACCURATE MONITORING OF X, Y, AND Z MAGNETIZATION FOR ANALYSIS

OF HARDWARE AND PULSE SEQUENCE PERFORMANCE IN NMR

SPECTROSCOPY

by

EMMALOU THERESA SCHMITTZEHE

A DISSERTATION

Presented to the Faculty of the Graduate School of the

MISSOURI UNIVERSITY OF SCIENCE AND TECHNOLOGY

In Partial Fulfillment of the Requirements for the Degree

DOCTOR OF PHILOSOPHY

in

CHEMISTRY

2019

Approved by:

Klaus Woelk, Advisor
Michael Van De Mark
Jeffrey Winiarz
Garry Grubbs
F. Scott Miller

ABSTRACT

A new nuclear magnetic resonance (NMR) imaging protocol has been developed to independently record the x, y, and z components of the nuclear net magnetization at any point in a pulse sequence while eliminating the observation of the other components. This protocol provides an experimental method of tracking magnetization which then can be used in conjunction with theoretical models to scrutinize the predicted outcome of each step in an NMR pulse sequence and potentially find further improvements to their effectiveness and efficiency. The protocol utilizes a rapid rotating-frame imaging pulse-train technique to obtain RF-field (B_1) and resonance-offset (ΔB_0) dependent profiles for each Cartesian component in the rotating magnetic coordinate system. The proposed protocol was used to analyze the distribution of the sample as a function of the B_1 field strength in a selective, single-channel ^1H probe as well as a standard, dual-channel broad-band probe. Data from both probes show that the magnetization within a sample is exposed to a wide range of B_1 field strength. Hard pulses of varying angles were examined showing that an expected pulse nutation angle, such as a 90° pulse, is only achieved for a very small portion of the sample. The protocol was also used to assess the performance of the widely used inversion-recovery sequence ($180° - \tau - 90°$) for spin-lattice relaxation measurements and to find improvements for the newly developed solvent-suppression sequence EXCEPT. Independently monitoring the magnetization components helped to identify that the remaining solvent-signal intensity after the EXCEPT sequence is linked to portions of the sample located in areas of very low and very high B_1 fields, leading to a targeted approach for improving the EXCEPT sequence.

ACKNOWLEDGMENTS

While many thanks are due, most is owed to my advisor for his many years of guidance and support. Thank you Dr. Woelk, I will be forever grateful. Although our similar tendencies for procrastination and the obsessive need for perfection has likely caused this to take longer than it could have, it also helped me grow as a researcher so that I can be successful in my career.

I would also like to thank Dr. Van de Mark, Dr. Winiarz, Dr. Grubbs, and Dr. Miller for serving on my committee. Thank you all for your patience and guidance throughout this process. Additionally, I want to express a very special thanks to Dr. Rex Gerald. I greatly appreciate your willingness to take the time to discuss experimental results and provide feedback on my writing; the combination of your NMR knowledge and perspective was immensely helpful.

Last but not least, I owe thanks to my family, friends, and group members that have encouraged me throughout the years. While I'm sure many others have had a positive impact on me getting this far, I extend my most sincere thanks to my parents, Katie, Josh, Evonne, Jackie, Travis, Amanda, Tyler, Lingyu, Ming, and Annalise. And finally, Chad, thank you for being there for me through all the stress and tears; I never would have finished if I didn't have a happy place to come home to.

.

TABLE OF CONTENTS

LIST OF ILLUSTRATIONS

LIST OF TABLES

NOMENCLATURE

Symbol	Description
NMR	Nuclear Magnetic Resonance
RF	radiofrequency
I	nuclear spin
α	α spin state
β	β spin state
ΔE	energy differnce between α and β spin states
$\hbar$	reduced Planck constant ($h/2\pi$)
γ	gyromagnetic ratio (magnetogyric ratio)
B_0	magnetic flux density (external magnetic field)
N_α	number of spins in the α state
N_β	number of spins in the β state
k	Boltzmann constant
T	absolute temperature
ν_L	nuclear precession frequency (Larmor frequency)
M_0	net magnetic moment at thermodynamic equilibrium
FID	Free Induction Decay
ADC	Analogue-to-Digital Converter
Δ	sampling interval (dwell time)
f_{max}	maximum frequency (Nyquist frequency)
B_1	oscillating magnetic field (radiofrequency field)

FT	Fourier Transformation
ΔB_0	deviation from the external field strength (resonance offset)
$\Delta \omega_0$	deviation from the nutation frequency
R	rotation matrix
θ	rotation angle
RIPT	Rapid Imaging Pulse Train
RFI	Rotating-Frame Imaging
ω_1	nutation frequency
n	number of data points
M_x	x component of the net magnetization
M_y	y component of the net magnetization
M_z	z component of the net magnetization
$M_x{}'$	x component of the net magnetization after an RF pulse
$M_y{}'$	y component of the net magnetization after an RF pulse
$M_z{}'$	z component of the net magnetization after an RF pulse
IR	Inversion-Recovery
τ	relaxation delay
T_1	longitudinal relaxation time constant (relaxation time)
M	signal intensity (net magnetic moment)
EXCEPT	EXponentially Converging Eradication Pulse Train
BTF	Biomass-To-Fuel

1. INTRODUCTION

1.1. NUCLEAR MAGNETIC RESONANCE SPECTROSCOPY

Nuclear magnetic resonance (NMR) spectroscopy is the study of the interaction of nuclei with radiofrequency (RF) electromagnetic radiation in the presence of an external magnetic field [1-4]. The interaction of nuclei with RF radiation depends on a property known as nuclear spin, which refers to the angular momentum of the nucleus. Nuclei with an odd number of protons and/or neutrons, such as ^{1}H and ^{13}C, possess a nonzero nuclear spin. A nucleus with nonzero spin results in a magnetic moment that will interact with an external magnetic field and therefore can be studied by NMR. In the absence of a magnetic field, nuclear magnetic moments are oriented randomly, whereas in the presence of an external magnetic field they align either with or against the field. For nuclei with spin I = ½, there are two possible orientations with respect to an external magnetic field, which are referred to as α spin state and β spin state. The α spin state corresponds to a lower energy level in which the spins are aligned more toward the direction of the external magnetic field. The β spin state corresponds to a higher energy state in which the spins are aligned more against the direction of the external field. The energy difference (ΔE) between the α and β spin states is directly proportional to the strength of the external magnetic field:

$$\Delta E = \hbar \gamma B_0 \tag{1}$$

where $\hbar$ is the reduced Planck constant ($\hbar = h/2\pi$), γ the gyromagnetic ratio of the nucleus, and B_0 the magnetic flux density at the location of the nucleus (external magnetic field).

The gyromagnetic ratio, sometimes called the magnetogyric ratio, is specific to a nucleus. For example, the gyromagnetic ratio of a ^{1}H nucleus is 42.58 MHz·T^{-1}, whereas a ^{13}C nucleus has a gyromagetic ratio of 10.71 MHz·T^{-1}. Because ΔE is small compared with the thermal energy of nuclei at room temperature, a considerable portion of the nuclei populate the higher energy spin state (β spin state). The ratio of nuclei in each spin state at thermodynamic equilibrium is defined by the Boltzmann distribution:

$$\frac{N_\beta}{N_\alpha} = e^{\left(-\frac{\Delta E}{kT}\right)} \tag{2}$$

where N_β is the number of spins in the β spin state, N_α is the number of spins in the α spin state, k is the Boltzmann constant, and T is the absolute temperature of the sample.

The magnetic moment of each spin precesses about the axis of the external magnetic field, B_0, at a frequency that is proportional to B_0:

$$\nu_L = \frac{\gamma B_0}{2\pi} \tag{3}$$

where ν_L is the nuclear precession frequency (Larmor frequency). At room temperature, the small excess of spins in the lower energy spin state (α spin state) results in a net magnetic moment, M_0, along the positive axis of the external magnetic field. The left side of Figure 1.1 displays a classical representation of the individual nuclear magnetic moments in a sample in the presence of an external magnetic field, and the right side shows the more commonly used representation of the resulting net magnetic moment. The net

magnetic moment is displayed as a vector in a magnetic coordinate system in which the z-axis, or the longitudinal axis, is defined to be directed along the direction of the external magnetic field.
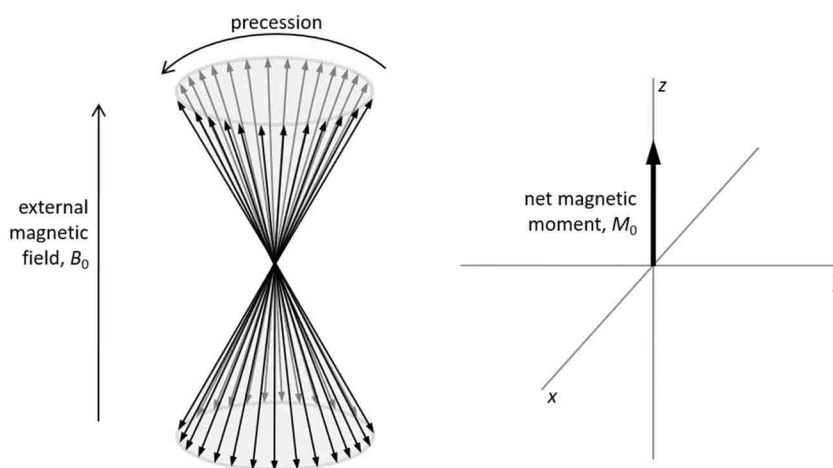
Figure 1.1. Classical representation of nuclear magnetic moments in the presence of an external magnetic field and the resulting net magnetic moment.

1.1.1. Hardware. A typical high-field NMR spectrometer consists of a superconducting magnet along with electronic components for pulse generation, signal acquisition, and magnetic field stabilization [5-7]. The major electronic components include coils and circuitry used to excite and detect the signal, a pulse programmer, and one or more radiofrequency channels. Each radiofrequency channel consists of a frequency synthesizer, a transmitter unit, a receiver unit, a power amplifier, and, if the spectrometer is not fully digital, a digitizer that converts the analog signal of the receiver into a digital signal that can be processed by a standard desktop computer or workstation. The superconducting magnet is constructed from a coil of wire material that has a resistance of zero when it is at low temperatures (typically less than 6 K), which means once a current

is set it persists without the need for additional electrical power. The continuous current creates a stable, static magnetic field perpendicular to the coil, which is referred to as the B_0 field. The low temperature is maintained by submersion of the coil in a bath of liquid helium cryogen at 4.2 K. To reduce the boil-off rate of the liquid helium, the helium bath is surrounded by a bath of liquid nitrogen at 77.2 K. The whole coil and cryogen baths assembly is mounted inside a vacuum chamber to further reduce heat loss.

At the center of the superconducting magnet is a vertical tube that is accessible from the outside so that a sample to be analyzed can be inserted. The vertical tube is typically positioned in the direction of the B_0 field. Inside the vertical tube is an exchangeable NMR probe that houses one or more coils to excite and detect the NMR signal. The probe coil is tuned to the resonance frequency of the nucleus of interest, or in case of a probe with more than one coil each may be tuned to a different frequency for multinuclear analysis. In addition to having the probe coil(s) tuned to an appropriate resonance frequency, it is important that the main magnetic field is as homogeneous as possible to minimize variations in the signal frequencies. Even with a set of superconducting shim coils, i.e., extra coils in the liquid helium bath used to homogenize the main magnetic field, the field of a superconducting magnet is typically not homogeneous enough for high-resolution NMR spectroscopy. Therefore, the homogeneity of the magnetic field is adjusted by a set of shim coils, each of which produce their own small magnetic field with various spatial profiles that are utilized to cancel out or add to portions of the main magnetic field to result in an overall homogenous field. Modern NMR spectrometers often have between 20 and 40 shim coils to adjust the homogeneity of the magnetic field, making the adjustment a complex task.

An NMR spectrometer is normally controlled by a pulse-program computer that communicates with but runs independently from the connected desktop computer. The pulse-program computer executes the pulse program specified by and downloaded from the desktop computer, and it is responsible for producing very precisely timed events (RF pulses and delays) that often occur in rapid succession. The pulses initiated by the pulse-program computer are generated by the transmitter. The transmitter consists of a "gated" RF source capable of producing a stable frequency and allowing the timing and length of pulses to be accurately controlled. A computer-controlled frequency synthesizer is used as the RF source, which makes it relatively easy not only to adjust the radiofrequency of the pulses but also to shift their phase. RF pulses created by the transmitter are passed through the probe coil to excite the sample. The same coil then acts as the receiver for the free induction decay (FID) signal. The voltage obtained from the receiver coil of the probe is converted to a binary code by the digitizer, also called the analogue-to-digital converter (ADC), and is stored in the computer memory. The ADC samples the voltage at regular intervals, resulting in an FID of discrete data points. The sampling rate of the ADC limits the maximum frequency (Nyquist frequency) that can be resolved by a discretely sampled FID [8,9]. With a sampling interval Δ, also called the dwell time, the Nyquist frequency, f_{max}, is given by the relationship:

$$f_{max} = \frac{1}{2\Delta} \tag{4}$$

A signal with a frequency greater than f_{max} (or less than $-f_{max}$) will still appear in the spectrum, but will be folded into the spectrum at a frequency that is the same number of Hertz from the edge of the spectrum as the true frequency is from f_{max} or $-f_{max}$.

1.1.2. RF Pulses. In NMR, an RF pulse is produced by passing an alternating current through the transmitter/receiver coil that surrounds the sample [10]. The result is an oscillating magnetic field, B_1, perpendicular to B_0, which leads to a rotation of the net magnetic moment about the B_1 axis. The phase of the B_1 field can be altered to adjust the direction of the B_1 field at any angle in the plane perpendicular to B_0. The most common phase settings result in B_1 fields along one of the transverse axes: $+x$, $+y$, $-x$, or $-y$. The rotation of the net magnetic moment about the B_1 axis is the consequence of population changes in the spin states α and β accompanied by a change in phase coherence of the nuclear spins, which alters the direction of the net magnetic moment while preserving the amplitude of net magnetic moment as shown in Figure 1.2.
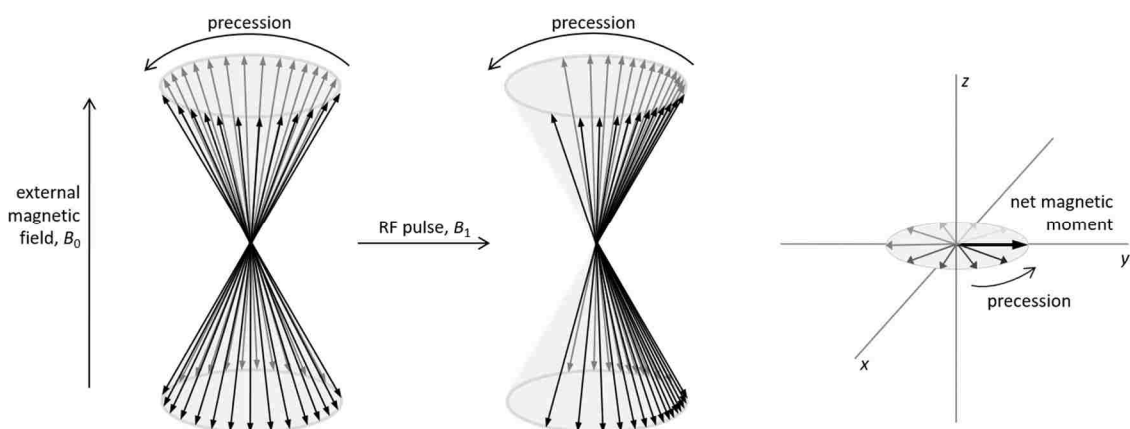
Figure 1.2. Changes in the spin state and phase coherence of the nuclear magnetic moments as a result of an RF pulse and the resulting net magnetic moment precessing in the transverse plane.

Just as the individual magnetic moments in a sample precess about the main magnetic field, the magnetic z-axis, any component of the net magnetic moment that is located in the magnetic xy-plane, or the transverse plane of the external magnetic field, precesses about the B_0 axis until it completely relaxes back to its thermodynamic equilibrium. The precession of the net magnetic moment in the transverse plane induces a current in the same coil that transmitted the RF signal to the sample (transmitter/receiver coil). The resulting coil voltage (typically in the sub-mV range) is amplified and converted to discrete data points by the ADC. Over time the signal decays as the net magnetic moment relaxes, resulting in the decay of the FID signal. The FID is then processed using a Fourier transformation (FT) procedure that converts the time-domain data to frequency-domain data; the result is an NMR spectrum of signal intensity versus resonance frequency. Signals at different frequencies are a result of magnetic moments precessing at different rates due to the actual magnetic field at the location of the particular nucleus; this gives rise to chemical-shift differences and resonance offsets from the incident RF transmitter frequency. Transmitter frequency offsets are denoted as ΔB_0, indicating the deviation from the field strength applied by the superconducting magnet.

1.1.3. Quadrature Detection. Both the x and y components of the magnetic moment must be known to distinguish between positive and negative deviations from the transmitter frequency ($\pm \Delta\omega_0 = \pm \gamma \Delta B_0$) [11]. One option to achieve the distinction is to sample data simultaneously along the x-axis and along the y-axis. However, the confined space of the probe and the difficulty in creating two electrically and magnetically isolated coils makes this a challenging task. An alternative that is more easily achieved involves mixing the received FID with locally generated frequencies that are phase-shifted by 90°.

This procedure splits the FID signal into two equal portions and feeds it into two separate mixers. The resulting outputs are equivalent to two orthogonal components, which are now identified as the x and y components in the rotating frame. The NMR software can adjust the receiver phases further to match the phase of the transmitted pulses.

1.2. ROTATION MATRICES

Rotation matrices are used to calculate the rotation of vectors, such as net magnetic moments, in a plane by a defined angle about the origin. This mathematical approach is useful to predict the effect of NMR pulses on magnetic moments of a single, independent resonance such as the ones studied in this research. For more complex spin systems where spin-spin coupling is involved, a more complex approach using density matrix theory must be used.

The rotation matrix (R) for a positive rotation by the angle θ according to the right-hand rule is:

$$R(\theta) = \begin{bmatrix} \cos\theta & -\sin\theta \\ \sin\theta & \cos\theta \end{bmatrix} \tag{5}$$

which rotates a vector by the angle θ counterclockwise about the origin. The rotation matrix for a negative rotation by the angle θ according to the right-hand rule is:

$$R(-\theta) = \begin{bmatrix} \cos(-\theta) & -\sin(-\theta) \\ \sin(-\theta) & \cos(-\theta) \end{bmatrix} = \begin{bmatrix} \cos\theta & \sin\theta \\ -\sin\theta & \cos\theta \end{bmatrix} \tag{6}$$

which rotates a vector by the angle θ clockwise about the origin. In order to utilize a rotation matrix, it is multiplied by the column vector that contains the components to be rotated. For instance, the positive rotation of the initial vector components (x_0, y_0) by θ is calculated as follows:

$$\begin{bmatrix} x \\ y \end{bmatrix} = \begin{bmatrix} \cos\theta & -\sin\theta \\ \sin\theta & \cos\theta \end{bmatrix} \begin{bmatrix} x_0 \\ y_0 \end{bmatrix} = \begin{bmatrix} x_0\cos\theta - y_0\sin\theta \\ x_0\sin\theta + y_0\cos\theta \end{bmatrix} \tag{7}$$

where the resulting column vector $\begin{bmatrix} x \\ y \end{bmatrix}$ corresponds to the components after the rotation (x, y). Similarly, the negative rotation of the initial components (x_0, y_0) by θ is calculated as follows:

$$\begin{bmatrix} x \\ y \end{bmatrix} = \begin{bmatrix} \cos\theta & \sin\theta \\ -\sin\theta & \cos\theta \end{bmatrix} \begin{bmatrix} x_0 \\ y_0 \end{bmatrix} = \begin{bmatrix} x_0\cos\theta + y_0\sin\theta \\ -x_0\sin\theta + y_0\cos\theta \end{bmatrix} \tag{8}$$

These rotations can be visualized in an xy-coordinate system as shown in Figure 1.3. In this figure, the thick blue arrow indicates the x component of the initial vector and the thin blue arrow indicates the result that contains both x and y components after the θ rotation. Similarly, the thick green arrow indicates the y component of the initial vector and the thin green arrow indicates the result that contains both x and y components after the θ rotation. The new x and y components of the rotated vector are obtained by adding together the resulting components from the rotation of each initial component. In the case of the positive rotation the x component is the sum of $x_0 \cdot \cos\theta$ and $-y_0 \cdot \sin\theta$ and the y component is the sum of $x_0 \cdot \sin\theta$ and $y_0 \cdot \cos\theta$, just as predicted by the rotation matrix

calculation. In the case of the negative rotation the x component is the sum of $x_0 \cdot \cos\theta$ and $y_0 \cdot \sin\theta$ and the y component is the sum of $-x_0 \cdot \sin\theta$ and $y_0 \cdot \cos\theta$, again as predicted by the rotation matrix calculation.

Positive rotation   **Negative rotation**
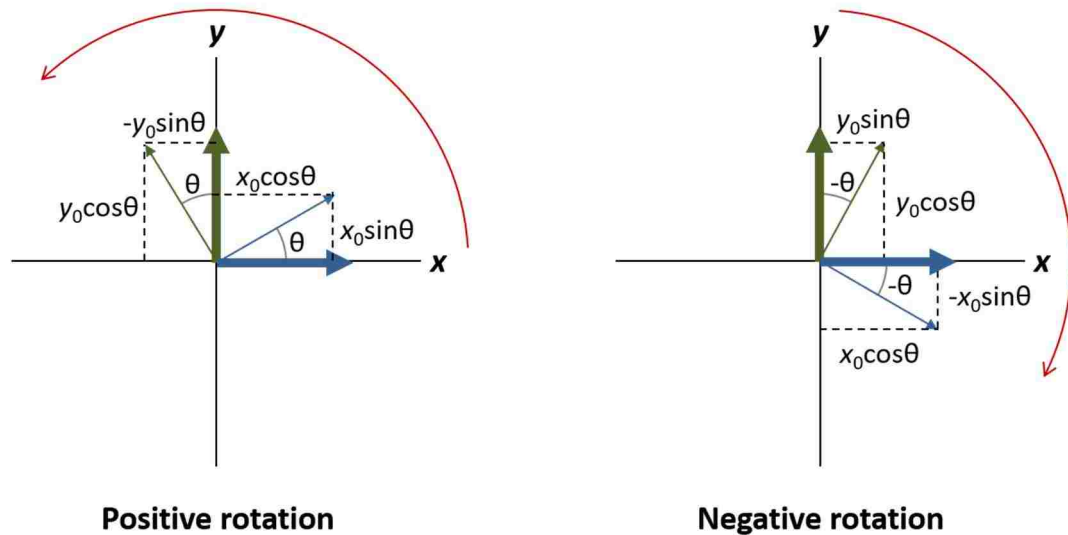
Figure 1.3. Positive and negative rotations of the x and y components of a sample vector.

The application of rotation matrices can be expanded from rotations within a plane to rotations in three-dimensional space. A three-dimensional rotation matrix rotates a vector by an angle about one of the three coordinate axes. Similar to the two-dimensional rotation matrices provided by Equations (5) and (6), the rotation matrices in Table 1.1 follow the right-hand rule where a positive rotation denotes a counterclockwise rotation about one of the coordinate axes and a negative rotation denotes a clockwise rotation about one of the coordinate axes. The rotation matrices are symbolized as R with a subscript that indicates the rotation axis and the angle of rotation denoted in parentheses.

Table 1.1. Standard rotation matrices for positive and negative rotations about x, y, and z axes.

Three-Dimensional Rotation Matrices	
Positive Rotation (counterclockwise)	**Negative Rotation (clockwise)**
$R_x(\theta) = \begin{bmatrix} 1 & 0 & 0 \\ 0 & \cos\theta & -\sin\theta \\ 0 & \sin\theta & \cos\theta \end{bmatrix}$	$R_x(\theta) = \begin{bmatrix} 1 & 0 & 0 \\ 0 & \cos\theta & \sin\theta \\ 0 & -\sin\theta & \cos\theta \end{bmatrix}$
$R_y(\theta) = \begin{bmatrix} \cos\theta & 0 & \sin\theta \\ 0 & 1 & 0 \\ -\sin\theta & 0 & \cos\theta \end{bmatrix}$	$R_y(\theta) = \begin{bmatrix} \cos\theta & 0 & -\sin\theta \\ 0 & 1 & 0 \\ \sin\theta & 0 & \cos\theta \end{bmatrix}$
$R_z(\theta) = \begin{bmatrix} \cos\theta & -\sin\theta & 0 \\ \sin\theta & \cos\theta & 0 \\ 0 & 0 & 1 \end{bmatrix}$	$R_z(-\theta) = \begin{bmatrix} \cos\theta & \sin\theta & 0 \\ -\sin\theta & \cos\theta & 0 \\ 0 & 0 & 1 \end{bmatrix}$

Three-dimensional rotation matrices are utilized in the same way as two-dimensional rotation matrices; the rotation is completed by multiplication of the rotation matrix by the column vector that represents the components to be rotated. For example, the positive rotation of the initial point (x_0, y_0, z_0) by θ about the x-axis is calculated as follows:

$$\begin{bmatrix} x \\ y \\ z \end{bmatrix} = \begin{bmatrix} 1 & 0 & 0 \\ 0 & \cos\theta & -\sin\theta \\ 0 & \sin\theta & \cos\theta \end{bmatrix} \begin{bmatrix} x_0 \\ y_0 \\ z_0 \end{bmatrix} = \begin{bmatrix} x_0 \\ y_0\cos\theta - z_0\sin\theta \\ y_0\sin\theta + z_0\cos\theta \end{bmatrix} \tag{9}$$

1.3. THE VECTOR MODEL

The vector model is used to provide a visual representation of the net magnetic moment (also referred to as net magnetization or bulk magnetization) throughout an NMR experiment. In this model the net magnetic moment is tracked within the magnetic coordinate system that defines the z-axis as the axis along the external magnetic field while the x- and y-axes lie perpendicular to the external magnetic field. A right-handed coordinate

system is used, meaning if the thumb of the right hand is pointed along the positive z-axis then the fingers of the right hand curl from the x-axis toward the y-axis. At the start of an NMR experiment when the nuclear spins are at thermodynamic equilibrium, the net magnetic moment, M_0, lies along the axis of the external magnetic field, B_0, as shown in Figure 1.4.
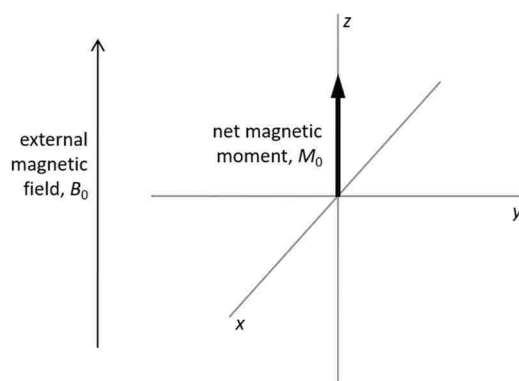
Figure 1.4. Vector model representation of the net magnetic moment, M_0, of a sample at thermodynamic equilibrium in the presence of an external magnetic field, B_0.

During an NMR experiment, the sample is exposed to radiofrequency pulses that cause the net magnetic moment to tip away from the z-axis. Just as the individual nuclear magnetic moments precess at the Larmor frequency counterclockwise about the external magnetic field, the net magnetic moment also precesses counterclockwise about the external magnetic field. This precession can complicate the visual representation of the net magnetization of a sample throughout an NMR experiment, therefore, the vector model is often drawn in terms of the rotating frame. In contrast to a coordinate system fixed in ordinary space (the laboratory frame) where the net magnetic moment precesses at the Larmor frequency, the rotating frame is a coordinate system understood to be rotating about

the *z*-axis at the Larmor frequency (Figure 1.5). The rotating frame allows the precessing

magnetic moment to be drawn in a fixed location. Unless otherwise noted, all vector model

representations in this dissertation will be in the rotating frame.
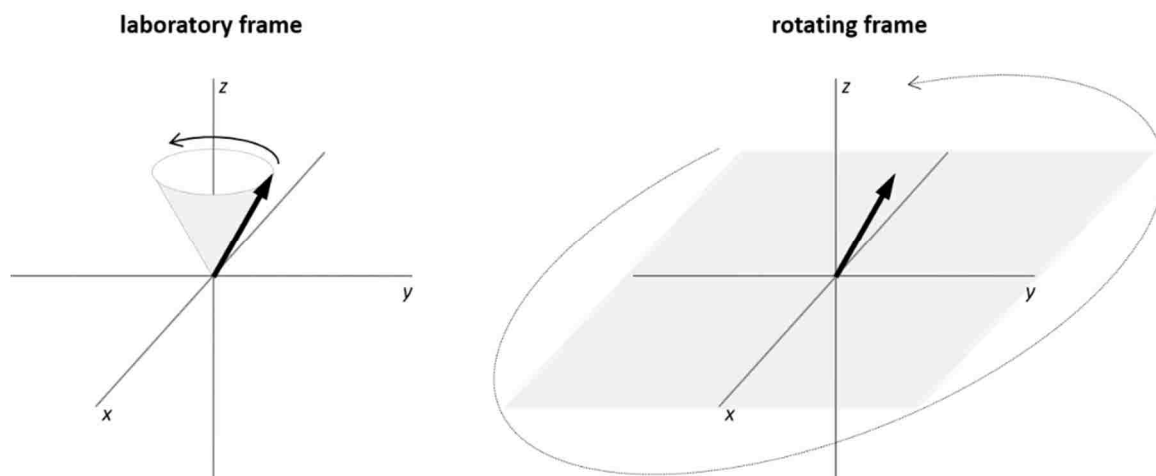
Figure 1.5. Vector model of a net magnetic moment in the laboratory frame versus a net
magnetic moment in the rotating frame.

2. RESEARCH JUSTIFICATION

NMR spectroscopy is most commonly used as a tool for structural identification of compounds, but it has many other applications and even extends to more complex studies such as molecular dynamics, conformational analysis of protein molecules, and imaging of the spatial distribution of spins [12,13]. In addition, NMR pulse sequences are continuously being designed to improve the current capabilities as well as to provide for new applications [14-16]. In this process theoretical methods such as visualizations of the net magnetic moment using the vector model, algebraic calculation methods using rotation matrices, and quantum mechanical methods using density matrix calculations represented by product operator formalism are utilized to predict the fate of the magnetization that will be observed with NMR. Although these theoretical methods are extremely useful to create and further develop experiments for measuring specific NMR parameters of interest, the newly created experiments often need further instrumental adjustment that cannot be predicted by current theories. NMR experimentalists are used to automatically adding transmitter and receiver phase cycling protocols as well as composite pulses or homospoil magnetic field gradients to compensate for common or unexpected signal artifacts in NMR spectra [17-20]. However, these somewhat experience-based solutions to known spectral artifacts can be complex, time consuming, insufficient, and in some cases can inadvertently create misleading data.

The results of NMR experiments can be impacted by several factors that are not accounted for in standard theoretical treatments. For instance, the reliability of NMR pulse sequences is critically dependent on the accuracy of the RF pulses with respect to timing,

phase stability, and amplitude stability. However, inaccuracies in the RF pulse performance are not always obvious, detectable, or predictable. Imperfections in the electronics that create the current for the RF pulse result in imperfections in the pulse shape, even when a pulse is "gated" on and off. These RF pulse shape imperfections lead to distortions in the predicted path of rotation of the net magnetic moment. Furthermore, the field created by an RF pulse cannot be assumed to be homogeneous across the entire sample, especially near the outer edges of the coil where the spins experience a weaker B_1 field. A weaker B_1 field will inadvertently result in smaller rotation angles compared to spins in a stronger B_1 field. Also, the rotation of the net magnetization due to RF pulses can be affected by inhomogeneities in the static magnetic field (B_0) leading to distortions in the expected path of rotation. In addition, an effect that could be included in theoretical calculations but is commonly ignored when designing pulse sequences is spin-spin and spin-lattice relaxation of the magnetization during RF pulses. Although it is often considered acceptable to ignore relaxation during short and strong RF pulses, relaxation effects on the resulting magnetization can have a significant effect on experimental results during long-lasting frequency-selective pulses [21,22].

This research aims to develop an experimental protocol that makes it possible to independently monitor the x, y, and z components of a net magnetic moment as a function of B_1 and ΔB_0. Separation of the individual components will help to improve theoretical predictions of the fate of magnetic moments during NMR pulse sequences. It can also be used to quickly and accurately assess the performance of known or newly designed NMR pulse sequences.

3. METHOD DEVELOPMENT

3.1. ISOLATION OF MAGNETIZATION COMPONENTS

Before getting to the complexities of imaging ΔB_0 and B_1 profiles, it is important to look at measuring individual component signals. Two things are necessary for this process: the component of interest must be in the observable xy-plane while the other two components must be cancelled. The x and y components are already in the observable plane, but the z component will require a 90° pulse to be placed in the observable plane. No matter which component is being acquired, there will have to be some type of RF pulse to cancel the other two components. For simplicity, 90° pulses will be used for all components. Furthermore, the right-hand rule for the physics of angular motion will be strictly followed, even though many textbooks use the left-hand rule when visualizing the performance of NMR pulse sequences.

There are four 90° transmitter phase options that will be considered, which correspond to the transverse axes of the rotating-frame magnetic coordinate system: $90°_{+x}$, $90°_{-x}$, $90°_{+y}$, and $90°_{-y}$. Figure 3.1 displays the vector-model representation of how each 90° pulse affects the x, y, and z components of magnetization; specifically, the magnetization components are each rotated 90° counterclockwise (right-hand rule) about the axis at which the RF transmitter field is located as denoted by the subscript to the pulse angle and the wave next to the corresponding axis. For example, the $90°_{+x}$ pulse rotates each magnetization component 90° counterclockwise about the $+x$-axis whereas the $90°_{-x}$ pulse rotates each magnetization component 90° counterclockwise about the $-x$-axis.
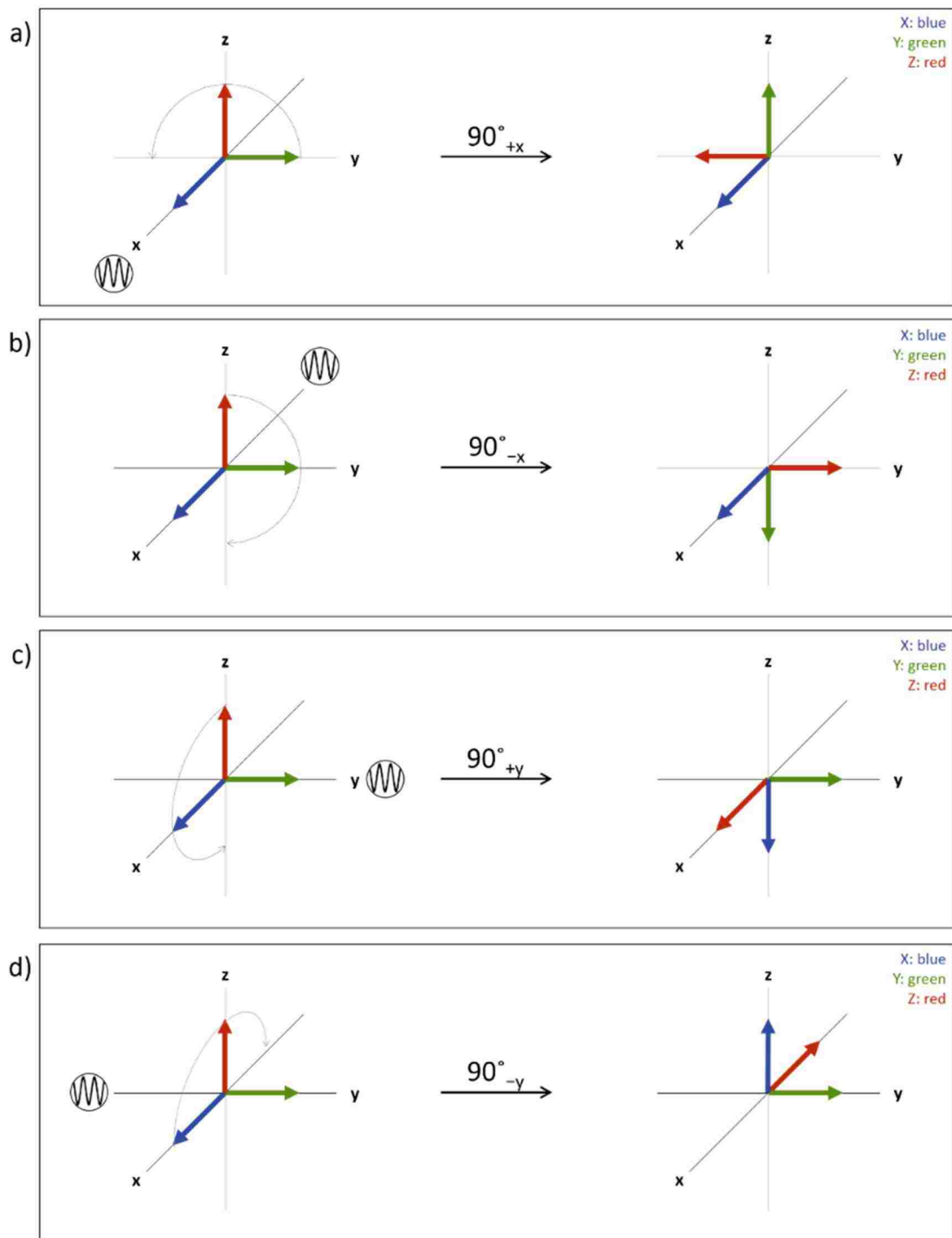
Figure 3.1. Vector model representations of how a 90° pulse affects the *x*, *y*, and *z* components of magnetization, rotating each component 90° counterclockwise about the RF transmitter phase axis. The transmitter phase is represented by a wave in each figure. a) Counterclockwise (positive) rotation about the *x*-axis for the $90°_{+x}$ pulse, b) clockwise (negative) rotation about the *x*-axis for the $90°_{-x}$ pulse, c) counterclockwise rotation about the *y*-axis for the $90°_{+y}$ pulse, and d) clockwise rotation about the *y*-axis for the $90°_{-y}$ pulse.

After each of these pulses there are four options for the receiver phase: $+x$, $-x$, $+y$, and $-y$. The choice of receiver phase determines which component is being observed in a given scan, while each transmitter/receiver phase combination corresponds to a single scan. To independently observe individual magnetization components two scans need to be combined to add the component of interest and cancel the other two components; therefore, two transmitter/receiver phase combinations that can be added together to isolate an individual component must be identified.

3.1.1. z Magnetization. When attempting to observe the z magnetization of a sample, the magnetization must be rotated into the plane where the receiver can record a signal, i.e., the transverse plane. For all of the possible transmitter phase options, a 90° pulse rotates the z component into the transverse plane. The receiver phase must be paired with the transmitter phase so that the rotated z component is observed. This means that the receiver phase must be set to $-y$ for a $+x$ transmitter phase, $+y$ for a $-x$ transmitter phase, $+x$ for a $+y$ transmitter phase, and $-x$ for a $-y$ transmitter phase. The left side of Figure 3.2 displays the results of the four possible 90° pulses, and each includes an eye next to the axis that corresponds to the necessary receiver phase to observe the rotated z component. The right side of Figure 3.2 displays a head-on view from the perspective of the selected receiver. When considering the need to cancel the rotated x and y components, the combination of two transmitter/receiver phase pairs can be selected; specifically, a $+x$ transmitter phase with a $-y$ receiver phase (Figure 3.2a) plus a $-x$ transmitter phase with a $+y$ receiver phase (Figure 3.2b) or a $+y$ transmitter phase with a $+x$ receiver phase (Figure 3.2c) plus a $-y$ transmitter phase with a $-x$ receiver phase (Figure 3.2d) will add the rotated z component and cancel the rotated x and y components.

Figure 3.2. Results of the four possible 90° pulses used for measurement of the *z* magnetization component on the left and a head-on view from the perspective of the receiver on the right. The receiver phase is represented by an eye in each figure. a) 90°$_{+x}$ pulse with a –*x* receiver phase, b) 90°$_{-x}$ pulse with a +*y* receiver phase, c) 90°$_{+y}$ pulse with a +*x* receiver phase, and d) 90°$_{-y}$ pulse with a –*x* receiver phase.

3.1.2. *y* Magnetization. When attempting to obtain the *y* magnetization signal only $90°_{+y}$ and $90°_{-y}$ pulses can be used for observation, because the $90°_{+x}$ and $90°_{-x}$ pulses would rotate the *y* magnetization out of the observable *xy*-plane. After these pulses the receiver phase must be set to the axis in which the *y* magnetization has been rotated, specifically, $+y$ for a $+y$ transmitter phase and $+y$ for a $-y$ transmitter phase. Figure 3.3 displays the results of the two possible 90° pulses, each with indication of the necessary receiver phase to observe the rotated *y* component, and a head-on view from the perspective of the receiver. The combination of these two transmitter/receiver phase pairs will successfully add the rotated *y* component and cancel the rotated *x* and *z* components.

Figure 3.3. Results of the two possible 90° pulses used for measurement of the *y* magnetization component on the left and a head-on view from the perspective of the receiver on the right. The receiver phase is represented by an eye in each figure. a) $90°_{+y}$ pulse with a $+y$ receiver phase and b) $90°_{-y}$ pulse with a $+y$ receiver phase.

3.1.3. *x* Magnetization.   Similar to the *y* magnetization, when attempting to obtain the *x* magnetization signal only 90°$_{+x}$ and 90°$_{-x}$ pulses can be used, because the 90°$_{+y}$ and 90°$_{-y}$ pulses would rotate the *x* magnetization out of the observable *xy*-plane. After these pulses the receiver phase is set to the axis in which the *x* magnetization has been rotated, specifically +*x* for the +*x* transmitter phase and +*x* for the −*x* transmitter phase. Figure 3.4 displays the results of the two possible 90° pulses, each with indication of the necessary receiver phase to observe the rotated *x* component, and a head-on view from the perspective of the receiver. The combination of these two transmitter/receiver phase pairs will successfully add the rotated *x* component and cancel the rotated *y* and *z* components.
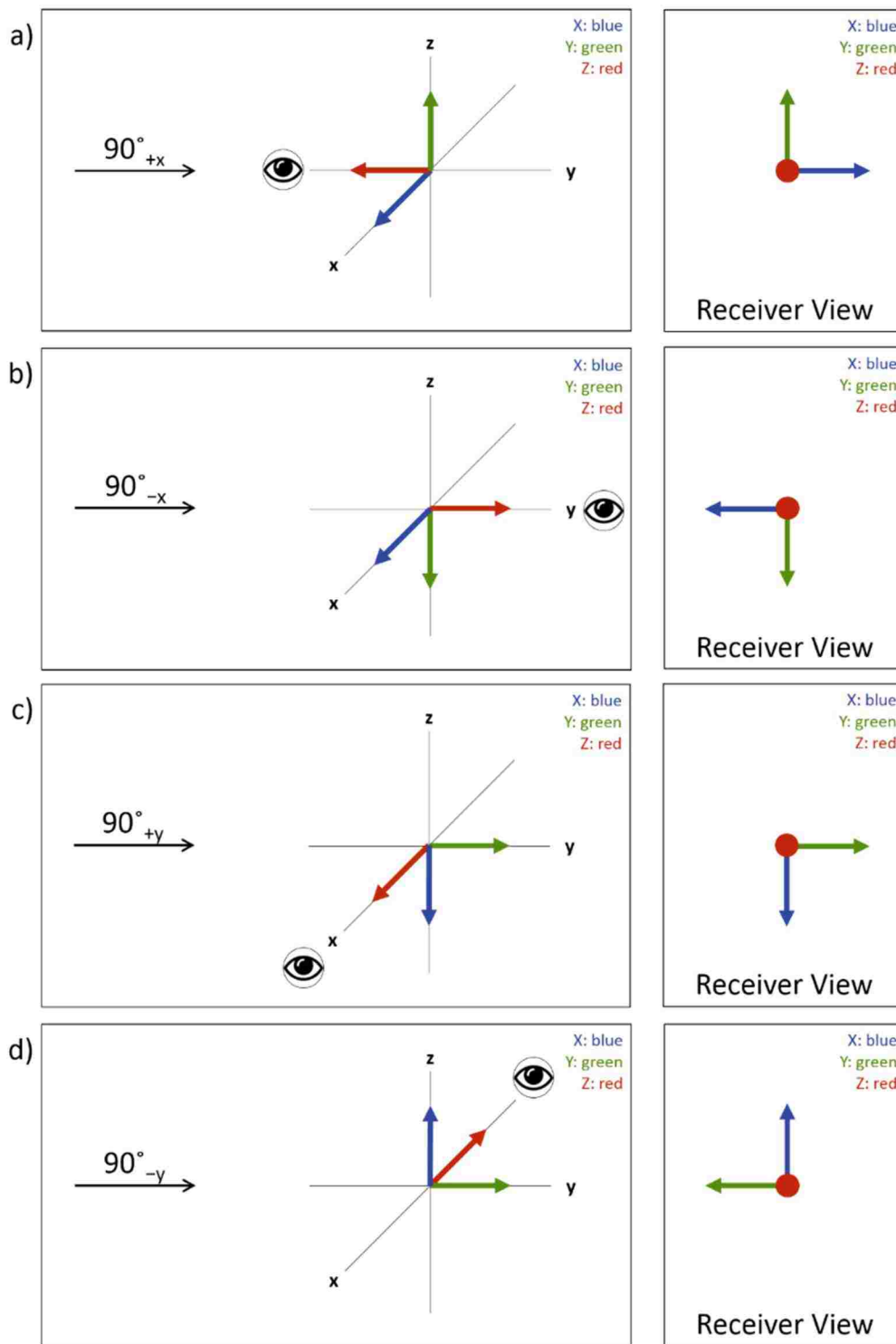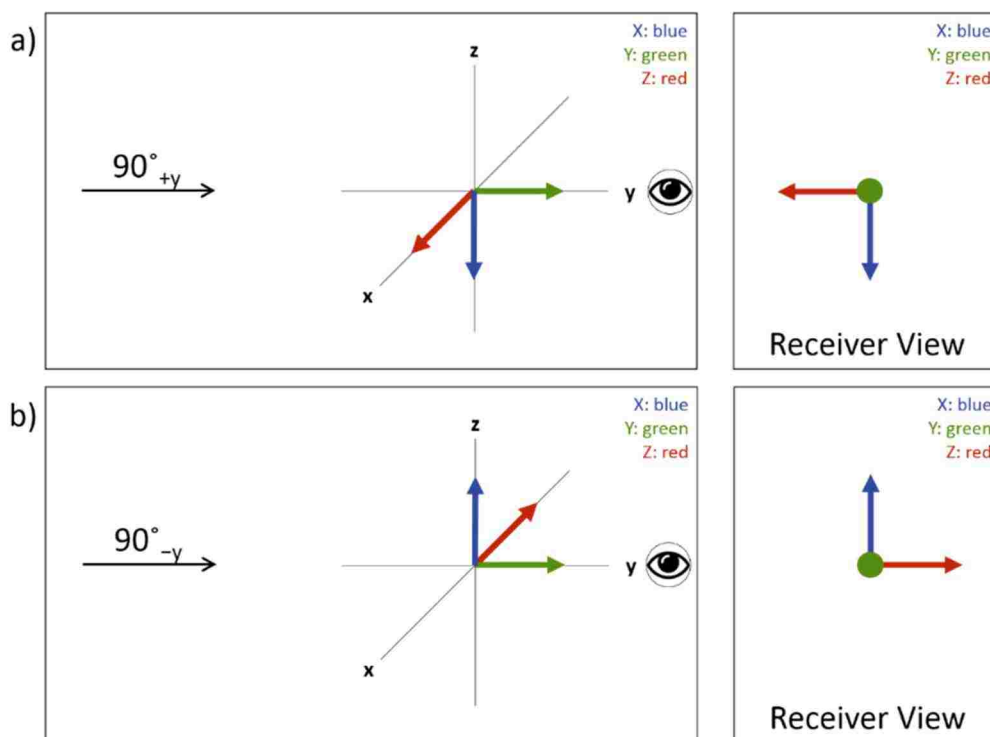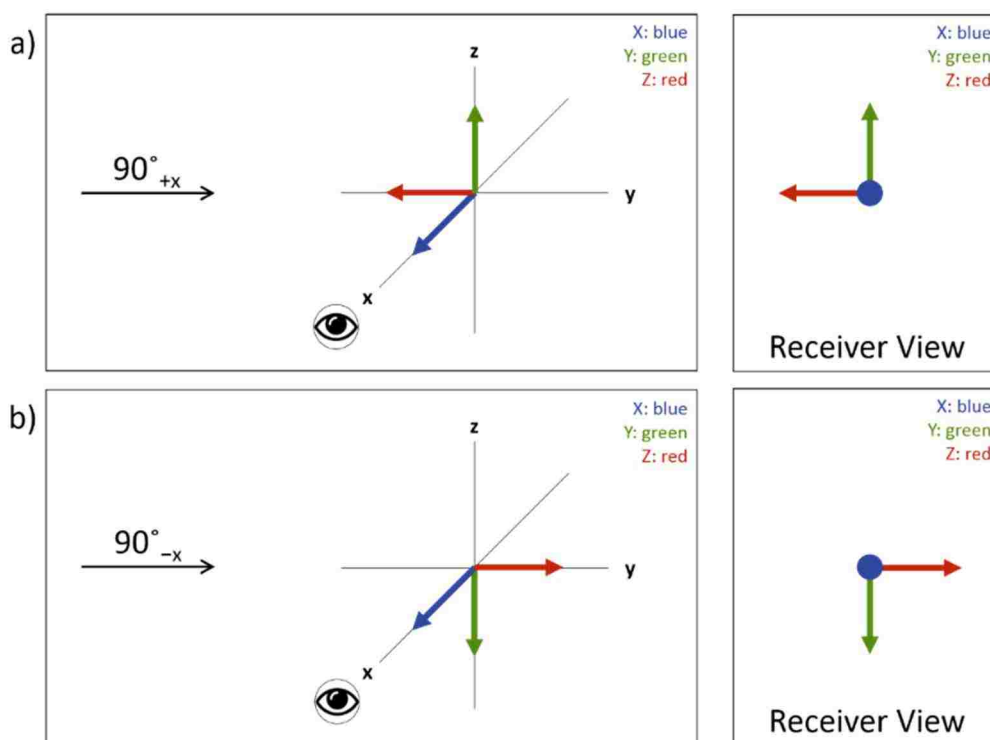

Figure 3.4. Results of the two possible 90° pulses used for measurement of the *x* magnetization component on the left and a head-on view from the perspective of the receiver on the right. The receiver phase is represented by an eye in each figure. a) 90°$_{+x}$ pulse with a +*x* receiver phase and b) 90°$_{-x}$ pulse with a +*x* receiver phase.

3.2. RAPID IMAGING PULSE TRAIN

The **R**apid **I**maging **P**ulse **T**rain (RIPT) experiment − originally termed: **R**apid rotating-frame **I**maging using an RF **P**ulse **T**rain – is an advanced, fast B_1 imaging technique to obtain one-dimensional B_1-dependent profiles [23]. Compared to traditional Rotating-Frame Imaging (RFI) [24], RIPT decreases the data-acquisition time significantly by collecting only a single data point where RFI records an entire FID. The single data-point acquisition eliminates the need to wait for relaxation of magnetization between successive data collections but comes at the expense of chemical-shift and J-coupling information. Sacrificing chemical-shift and J-coupling information may be acceptable when a known sample of only one spectral feature is investigated or where chemical-shift and J-coupling information is not desired. However, for advanced studies involving spectra of multiple peaks, chemical-shift-selective versions of RIPT using frequency-selective pulses or difference spectroscopy have been proposed cancelling all but the desired resonance [23,25].

The RIPT sequence (Figure 3.5a) begins with the collection of a single data point (or a single complex data point if quadrature detection is enabled) followed by a short RF pulse. Immediately thereafter a second single data point is collected, and another short RF pulse of equal power and duration applied. The single data-point collection and RF pulse application is repeated until the number of data points defined in the experiment has been acquired. The RIPT procedure generates amplitude-modulated interferogram data of B_1-dependent nutation frequencies (Figure 3.5b), which are referred to in the early literature as a "pseudo FID" [26] or "driven FID" [23]. A standard Fourier transformation of the interferogram data, or a real-only Fourier transformation when complex data points are

collected, yields a profile of signal intensities versus pulse-angle dependent nutation frequencies (ω_1) without resolving chemical-shift and J-coupling information.
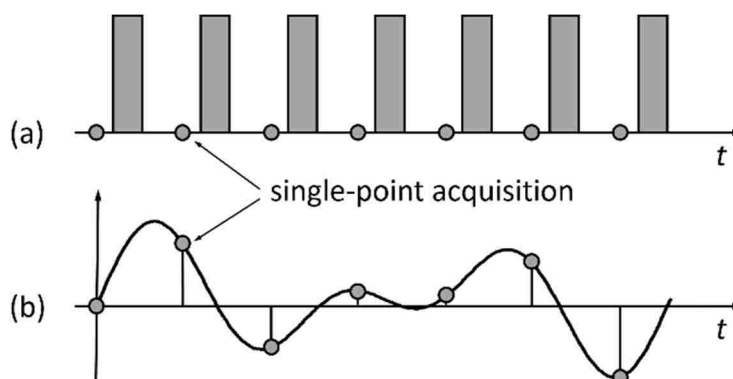
Figure 3.5. Schematic representations of a) the Rapid rotating-frame Imaging Pulse Train (RIPT) which involves a train of short rectangular RF pulses with intermittent single-point data acquisitions and b) an interferogram of B_1-dependent nutation frequencies recorded by the RIPT sequence.

The frequency-domain profile obtained from a Fourier transformation of the obtained interferogram can easily be converted into a B_1-dependent profile using the equation:

$$\omega_1 = \gamma B_1 \tag{10}$$

which connects the nutation frequency, ω_1, mathematically to the RF field strength, B_1.

3.3. MAGNETIZATION COMPONENT PROFILES

Instead of applying 90° pulses to acquire the individual magnetization component signals, a RIPT sequence is applied to acquire B_1-field dependent profiles for each of the components. Since the RIPT sequence involves multiple pulses throughout the collection

of data, a visual representation using the vector model may not always be as convincing as in the case of the simple 90° pulse experiments. To show that only one component remains when appropriate RIPT experiments are added while all other components cancel or, at a minimum, do not contribute to the B_1-dependent profiles, a mathematical representation was chosen in addition to the visualization. This mathematical representation involves the application of standard three-dimensional rotation matrices (Table 1.1) to determine the location of the net-magnetization components.

Table 3.1 shows the calculations of the x, y, and z components after each RIPT pulse, where θ corresponds to the nutation angle achieved by a single pulse in the RIPT sequence. Similar to the 90° pulse experiments, there are four possible transmitter phases with which the RIPT sequence can be executed: $+x$, $-x$, $+y$, and $-y$, which are designated as subscripts to RIPT, i.e., $RIPT_{+x}$, $RIPT_{-x}$, $RIPT_{+y}$, and $RIPT_{-y}$. Although the RIPT sequence consists of a series of short pulses with single data points collected during the interpulse period, the transmitter and receiver phase settings remain constant throughout the entire sequence. Because data points are recorded before the application of each individual RIPT pulse, the cumulative RIPT nutation angle at the conclusion of the sequence is $(n-1)\times\theta$, where n is the number of data points collected with the RIPT sequence. The M_x, M_y, and M_z represent the initial components of the magnetization before the RIPT sequence and M_x', M_y', and M_z' the resulting components after a single RIPT pulse application. Furthermore, the M_x' and M_y' components correspond to the signals that are observed when the receiver phase is placed in the $+x$ and $+y$ direction, respectively. Multiplying the transverse components M_x' and M_y' by -1 corresponds to the signals that are observed when the receiver phase is in the $-x$ and $-y$ direction, respectively. Since only

the transverse components M_x' and M_y' can be observed by NMR, the M_z' component will be ignored for the majority of the future analysis.

Table 3.1. Magnetization vector calculations for the RIPT sequence using a θ pulse angle about the $+x$, $-x$, $+y$, and $-y$ axes.

RIPT$_{+x}$	$\begin{bmatrix} M_x' \\ M_y' \\ M_z' \end{bmatrix} = \begin{bmatrix} 1 & 0 & 0 \\ 0 & \cos\theta & -\sin\theta \\ 0 & \sin\theta & \cos\theta \end{bmatrix}\begin{bmatrix} M_x \\ M_y \\ M_z \end{bmatrix} = \begin{bmatrix} M_x \\ M_y\cos\theta - M_z\sin\theta \\ M_y\sin\theta + M_z\cos\theta \end{bmatrix}$
RIPT$_{-x}$	$\begin{bmatrix} M_x' \\ M_y' \\ M_z' \end{bmatrix} = \begin{bmatrix} 1 & 0 & 0 \\ 0 & \cos\theta & \sin\theta \\ 0 & -\sin\theta & \cos\theta \end{bmatrix}\begin{bmatrix} M_x \\ M_y \\ M_z \end{bmatrix} = \begin{bmatrix} M_x \\ M_y\cos\theta + M_z\sin\theta \\ -M_y\sin\theta + M_z\cos\theta \end{bmatrix}$
RIPT$_{+y}$	$\begin{bmatrix} M_x' \\ M_y' \\ M_z' \end{bmatrix} = \begin{bmatrix} \cos\theta & 0 & \sin\theta \\ 0 & 1 & 0 \\ -\sin\theta & 0 & \cos\theta \end{bmatrix}\begin{bmatrix} M_x \\ M_y \\ M_z \end{bmatrix} = \begin{bmatrix} M_x\cos\theta + M_z\sin\theta \\ M_y \\ -M_x\sin\theta + M_z\cos\theta \end{bmatrix}$
RIPT$_{-y}$	$\begin{bmatrix} M_x' \\ M_y' \\ M_z' \end{bmatrix} = \begin{bmatrix} \cos\theta & 0 & -\sin\theta \\ 0 & 1 & 0 \\ \sin\theta & 0 & \cos\theta \end{bmatrix}\begin{bmatrix} M_x \\ M_y \\ M_z \end{bmatrix} = \begin{bmatrix} M_x\cos\theta - M_z\sin\theta \\ M_y \\ M_x\sin\theta + M_z\cos\theta \end{bmatrix}$

As with the simpler x, y, and z component examples (see Sections 3.1.1 to 3.1.3), a series of two scans in which the desired component will add while the others will be eliminated is needed. This will again involve an appropriate selection of transmitter and receiver phase pairs for each scan. However, when using the RIPT sequence to obtain interferograms of the individual components, it is important to realize that data modulated by the ω_1 nutation frequency can only be collected if transmitter and receiver are phase-shifted by 90°. The 90° phase shift is required because magnetization along the axis of the RF field, or 180° phase shifted to the axis of the RF field, will not be amplitude-modulated by ω_1 but will remain unchanged along the transmitter axis. In other words, if the receiver phase is set along the same axis as the transmitter phase, a constant signal intensity is

recorded that will eventually decay because of transverse relaxation. This is evident from the calculations, which show that the M_x' component remains M_x for both a RIPT$_{+x}$ and a RIPT$_{-x}$ pulse, and M_y' remains M_y for both a RIPT$_{+y}$ and a RIPT$_{-y}$ pulse. All other components, i.e., where transmitter and receiver are phase-shifted by 90°, show the desired sinθ and cosθ modulation that will result in the desired ω_1 interferograms to yield B_1-field dependent profiles.

Further analysis of the matrix calculation results reveals combinations that will allow the addition of one θ-modulated component while eliminating the other components. Table 3.2 provides a summary of the magnetization components after a RIPT$_{+x}$, RIPT$_{-x}$, RIPT$_{+y}$, and RIPT$_{-y}$ pulse, where the M_x', M_y', $-M_x$', and $-M_y$' components correspond to observations with the $+x$, $+y$, $-x$, and $-y$ receiver phases, respectively. The red arrows indicate combinations of transmitter and receiver phase settings that will add one modulated component and cancel the other. After the x-phase RIPT pulses (RIPT$_{+x}$ or RIPT$_{-x}$) the M_y' component, which would be observed with the $+y$ or $-y$ receiver phases, is composed of a mixture of θ-modulated original M_y and M_z components. Adding the results of a scan with a $+x$ transmitter phase and $-y$ receiver phase to the results of a scan with a $-x$ transmitter phase and $+y$ receiver phase will cancel the y component and add the z component, while adding the results of a scan with a $+x$ transmitter phase and $+y$ receiver phase with the results of a scan with a $-x$ transmitter phase and $+y$ receiver phase will add the y component and cancel the z component. Similarly, after the y-phase RIPT pulses (RIPT$_{+y}$ or RIPT$_{-y}$), the M_x' component, which would be observed with the $+x$ or $-x$ receiver phases, is composed of a mixture of θ-modulated original M_x and M_z components. Again, an appropriate combination of transmitter and receiver phases can be used to

observe either M_x or M_z while the respective other component is cancelled. Specifically, the combination of a $+y$ transmitter phase with $+x$ receiver phase and a $-y$ transmitter phase with $-x$ receiver phase will cancel the x component and add the z component, whereas the combination of a $+y$ transmitter phase with $+x$ receiver phase and a $-y$ transmitter phase with $+x$ receiver phase will add the x component and cancel the z component.

Table 3.2. Summary of the resulting magnetization components after a RIPT$_{+x}$, RIPT$_{-x}$, RIPT$_{+y}$, and RIPT$_{-y}$ pulse, where the subscript $+x$, $-x$, $+y$, and $-y$ correspond to the transmitter phase of the RIPT sequence, and the $M_x{'}$, $M_y{'}$, $-M_x{'}$, and $-M_y{'}$ components correspond to observations with the receiver phase set to $+x$, $+y$, $-x$, and $-y$, respectively. Appropriate sets of transmitter and receiver phase pairs that will add one θ-modulated component and cancel the other are indicated by the red arrows.

Rotation	$\begin{bmatrix} M_x{'} \\ M_y{'} \end{bmatrix}$ (observation from positive axes)	$\begin{bmatrix} -M_x{'} \\ -M_y{'} \end{bmatrix}$ (observation from negative axes)
RIPT(θ)$_{+x}$	$\begin{bmatrix} M_x \\ M_y \cos\theta - M_z \sin\theta \end{bmatrix}$	$\begin{bmatrix} -M_x \\ -M_y \cos\theta + M_z \sin\theta \end{bmatrix}$
RIPT(θ)$_{-x}$	$\begin{bmatrix} M_x \\ M_y \cos\theta + M_z \sin\theta \end{bmatrix}$	$\begin{bmatrix} -M_x \\ -M_y \cos\theta - M_z \sin\theta \end{bmatrix}$
RIPT(θ)$_{+y}$	$\begin{bmatrix} M_x \cos\theta + M_z \sin\theta \\ M_y \end{bmatrix}$	$\begin{bmatrix} -M_x \cos\theta - M_z \sin\theta \\ -M_y \end{bmatrix}$
RIPT(θ)$_{-y}$	$\begin{bmatrix} M_x \cos\theta - M_z \sin\theta \\ M_y \end{bmatrix}$	$\begin{bmatrix} -M_x \cos\theta + M_z \sin\theta \\ -M_y \end{bmatrix}$

Figure 3.6 displays the vector-model representation for the first few data points of RIPT sequence performed with the four standard transmitter phases ($+x$, $-x$, $+y$, and $-y$) as well as the corresponding x and y component values calculated using rotation matrices. The displayed vectors correspond to the orientation of the magnetization components at a time when the first few data points are collected, with the bold arrow indicating the furthest progression shown. Accordingly, each magnetization component perpendicular to the incident RF field is progressed successively by θ, while magnetization components along

the RF transmitter axis are stationary. The nutation process would continue further until

the desired number of data points is recorded. As a result, the net magnetization is often

rotated several hundred times about the transmitter axis during a RIPT sequence.
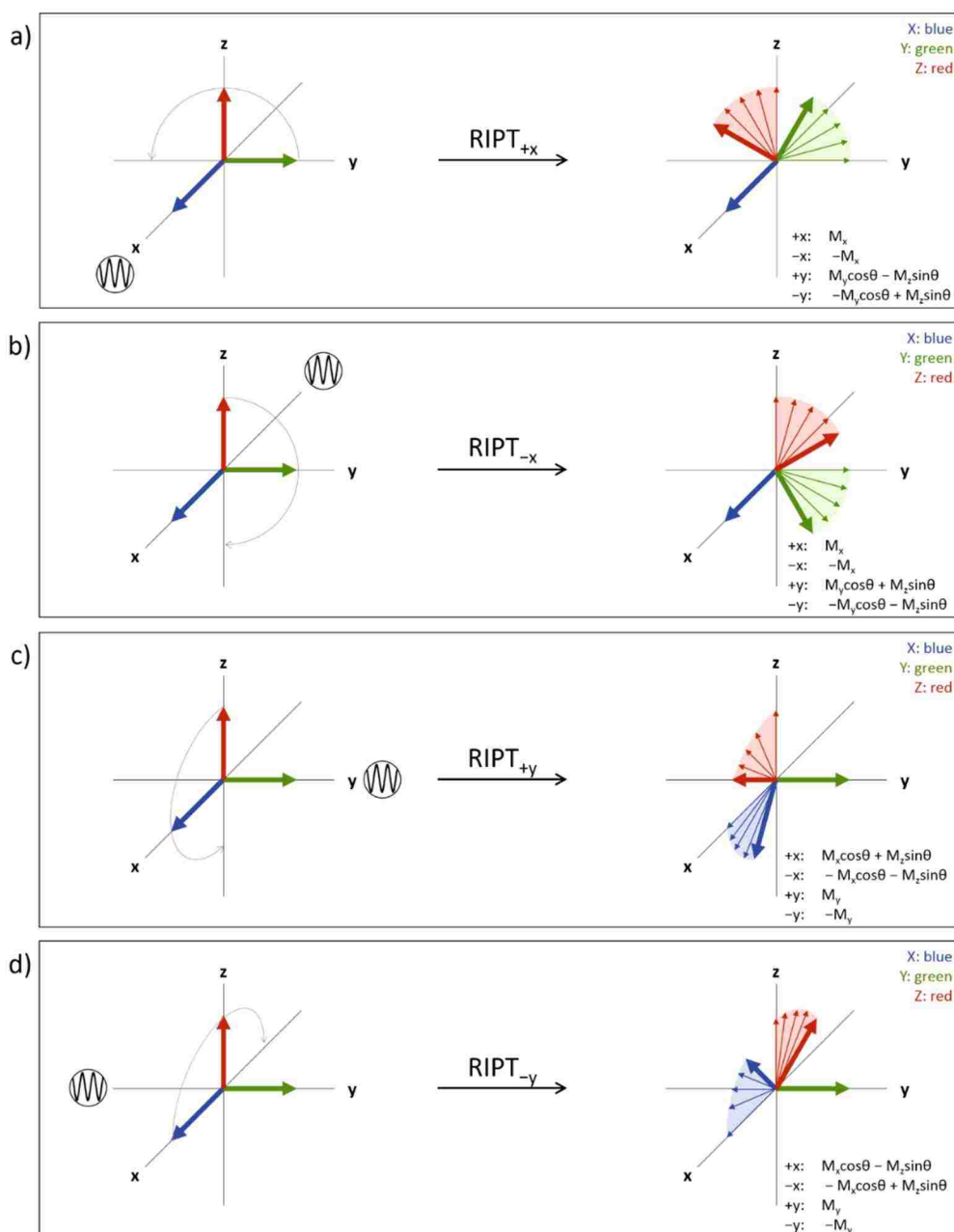
Figure 3.6. Vector model representation for the first few data points of the a) RIPT$_{+x}$, b) RIPT$_{-x}$, c) RIPT$_{+y}$, and d) RIPT$_{-y}$ sequence. The corresponding *x* and *y* component values are listed with each vector representation.

3.3.1. *z* Magnetization. As mentioned above, there are two possible sets of transmitter/receiver phase pairs that can be used to obtain the *z* magnetization component: +*x*/–*y* and –*x*/+*y* or +*y*/+*x* and –*y*/–*x*. Figure 3.7 displays the vector diagrams for each of these transmitter/receiver phase pairs.
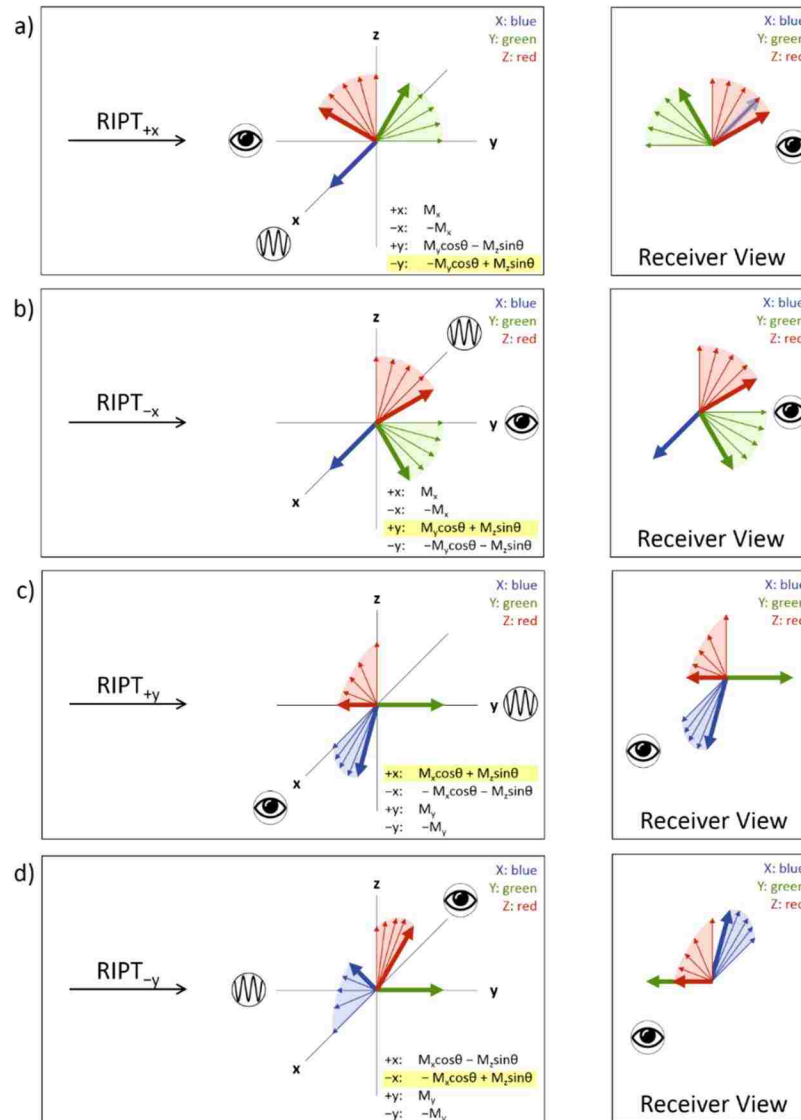
Figure 3.7. Vector diagrams for the transmitter/receiver phase pairs that can be used for the measurement of the *z* magnetization component (left) and the corresponding receiver view (right). a) +*x* transmitter phase and –*y* receiver phase, b) –*x* transmitter phase and +*y* receiver phase, c) +*y* transmitter phase and +*x* receiver phase, and d) –*y* transmitter phase and –*x* receiver phase.

The right side of Figure 3.7 shows the receiver view for each scan, but the scans observed from the negative axes have been rotated about the *z*-axis to allow viewing from the same perspective compared to the scans observed from the positive axes. In each set (Figure 3.7a and b, and Figure 3.7c and d) the ($n\times\theta$)-modulated *z* components add while the modulated *x* and *y* components cancel. The same result is achieved mathematically by adding the highlighted components obtained from the rotation matrix calculations.

3.3.2. *y* Magnetization. As depicted above, only one set of transmitter/receiver phase pairs exists that can be used to obtain the θ-modulated *y* magnetization component: +*x*/+*y* and –*x*/+*y*. Figure 3.8 displays the vector diagrams for these transmitter/receiver phase pairs along with the receiver phase and the calculated magnetization highlighted.
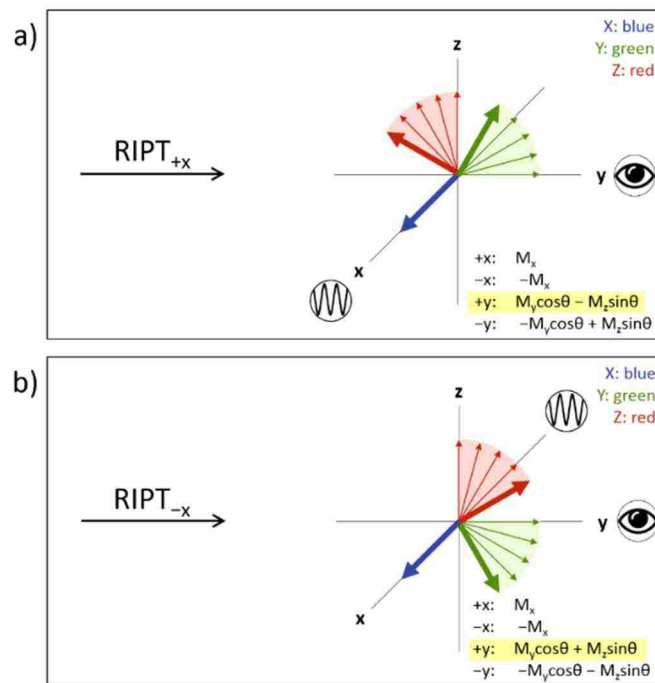

Figure 3.8. Vector diagrams for the transmitter/receiver phase pairs that are used for the measurement of the *y* magnetization component. a) +*x* transmitter phase and +*y* receiver phase and b) –*x* transmitter phase and +*y* receiver phase.

In Figure 3.8 the ($n \times \theta$)-modulated y components add while the modulated z components cancel, which is also seen mathematically by the addition of the highlighted components. It is noted, however, that the unmodulated x component remains in the same position with respect to the receiver phase and is not canceled. Still this component should not become part of the recorded signal since it is orthogonal (perpendicular) to the receiver phase and, in addition, it is not modulated by the angle θ.

3.3.3. x Magnetization. As shown above, only one set of transmitter/receiver phase pairs exists that can be used to obtain the θ-modulated x magnetization component: $+y/+x$ and $-y/+x$. Figure 3.9 displays the vector diagrams for each of these transmitter/receiver phase pairs along with the receiver phase and the calculated magnetization highlighted.
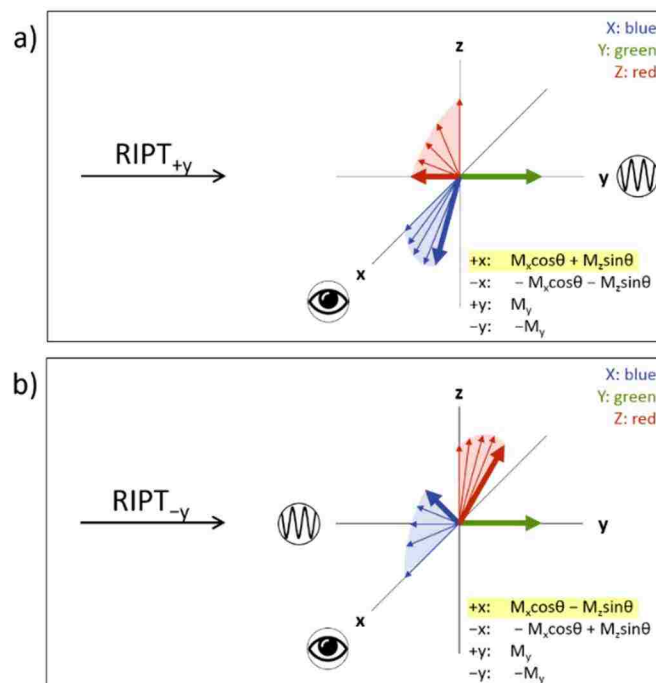
Figure 3.9. Vector diagrams for each transmitter/receiver phase pair that are used for the measurement of the x magnetization component. a) $+y$ transmitter phase and $+x$ receiver phase and b) $-y$ transmitter phase and $+x$ receiver phase.

In Figure 3.9 the $(n \times \theta)$-modulated x components add while the modulated z components cancel, which is also seen mathematically by the addition of the highlighted components. Similar to the observation of the θ-modulated y component, during the observation of the θ-modulated x component a perpendicular unmodulated component (here, the y component) remains but should not become part of the observed signal.

4. RESULTS AND DISCUSSION

All NMR experiments were carried out at room temperature using a Bruker Avance DRX-200 wide-bore spectrometer. The hard-pulse experiments were conducted on a 1:1 mixture of chloroform and deuterated chloroform in a 5-mm NMR tube employing a selective, single-channel ^{1}H probe. Probe performance experiments were conducted with the same sample using a selective, single-channel ^{1}H probe and a standard, dual-channel broadband probe. The inversion-recovery and EXCEPT solvent-suppression experiments were conducted using the selective, single-channel ^{1}H probe on a sample consisting of a 1:9 mixture of water and deuterated water in a 5-mm NMR-tube. The water/deuterated water sample was doped with trace amounts of copper(II) sulfate ($CuSO_4$) to adjust the longitudinal relaxation time, T_1, to 1.7 seconds.

4.1. HARD PULSE EXPERIMENTS

The developed protocol was implemented to monitor the fate of the magnetization components during a simple hard-pulse excitation. The experiments to independently monitor the x, y, and z components of the magnetization were conducted on a sample of chloroform in deuterated chloroform, which contains only one ^{1}H resonance. This allowed the simple measurement of B_1 profiles of the sample on resonance as well as B_1 profiles with resonance offsets ranging from -5 kHz to +5 kHz.

As a reference, the components of the net magnetization at thermodynamic equilibrium (0° or no pulse) were measured first. The experimentally observed x, y, and z components were used to construct three-dimensional magnetization vectors that were then

mapped as a function of B_1 field strength and ΔB_0 resonance offset as shown in Figure 4.1.

It is important to note that there is no difference in the results with respect to ΔB_0 because

no preparation pulse was applied to the sample prior to the execution of the RIPT sequence.

The resulting profiles show that the magnetic moments in the sample experience a wide

range of B_1 field strength; while a large portion is exposed to a relatively strong B_1 field,

there is still a significant portion of the sample exposed to a wide range of lower B_1 field.
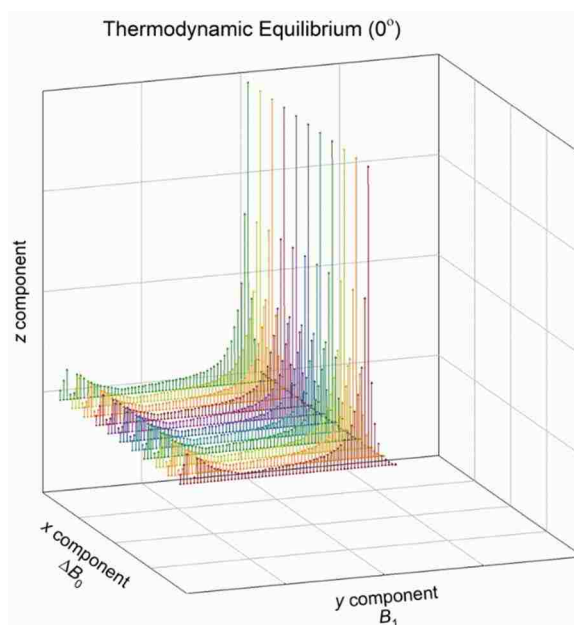
Figure 4.1. Net magnetization at thermodynamic equilibrium as a function of B_1 field and ΔB_0 resonance offset.

Similar experiments were conducted on the same sample to measure each

component of the net magnetization after a nominal $15°_{+x}$ hard pulse, $30°_{+x}$ hard pulse,

$45°_{+x}$ hard pulse, $60°_{+x}$ hard pulse, $75°_{+x}$ hard pulse, and $90°_{+x}$ hard pulse (Figure 4.2). The

nominal pulse angles were determined from a standard pulse-width dependent B_1 nutation

experiment, where the pulse width leading to the maximum signal intensity was identified as the nominal 90° pulse.

Figure 4.2. Net magnetization vectors after a nominal $15°_{+x}$, $30°_{+x}$, $45°_{+x}$, $60°_{+x}$, $75°_{+x}$, and $90°_{+x}$ hard-pulse experiment as a function of B_1 field strength and ΔB_0 resonance offset.

There was no significant difference in the pulse performance with respect to the resonance offset ΔB_0 between the different nominal pulse nutation angles; however, substantial deviations fr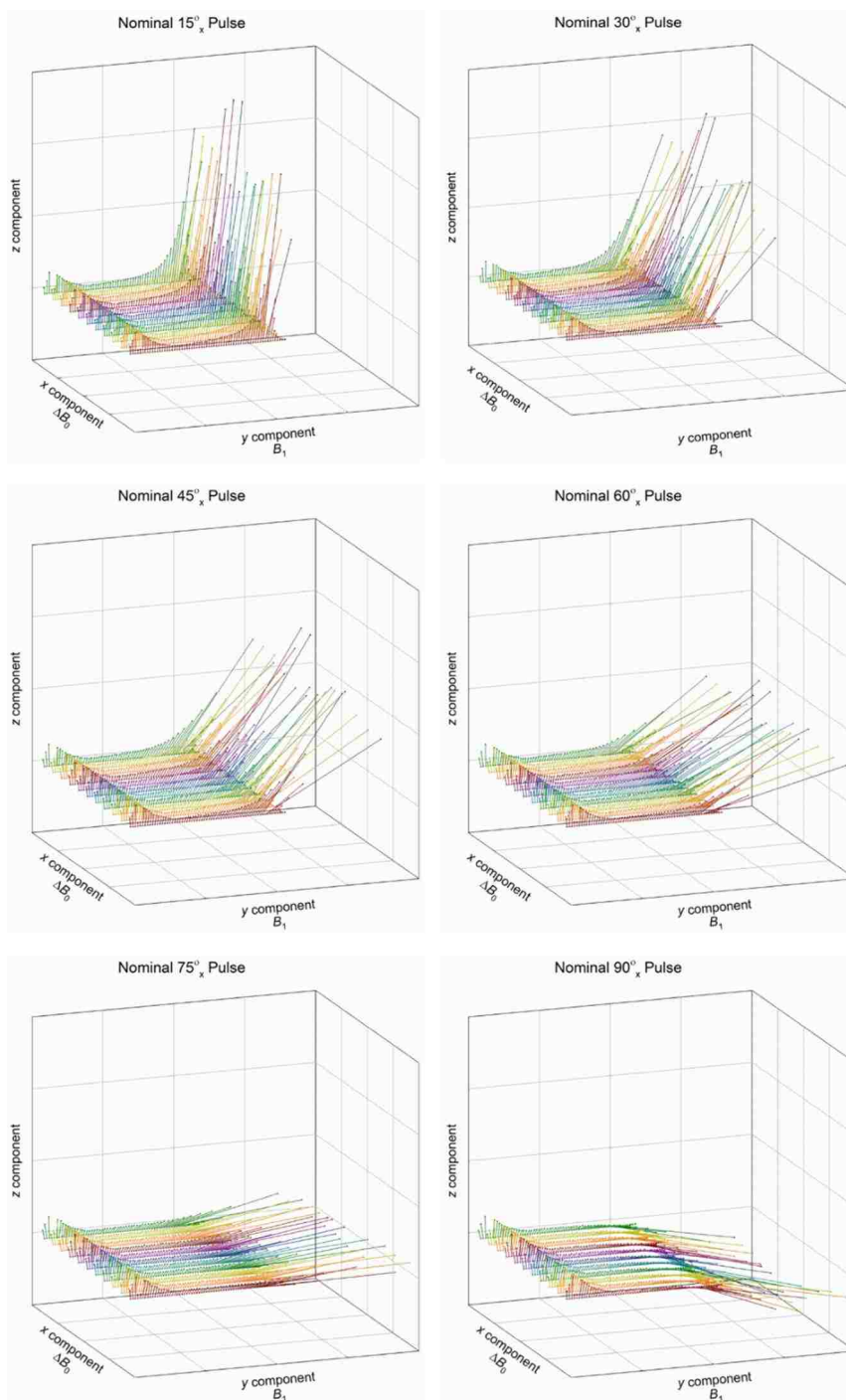om the ideal nutation as a function of B_1 field strength were observed. For instance, a $90°_{+x}$ pulse would ideally rotate the z component of the magnetization by 90° about the x-axis, resulting in a magnetization that consists only of a y component. However, the data from the $90°_{+x}$ experiment shows that there is a significant portion of the magnetization rotated more or less than 90°. Considering that the thermodynamically equilibrated magnetization is exposed to a wide range of B_1 field (Figure 4.1), it makes sense that not all of the magnetization is rotated the same amount. The magnetic moments in areas of low B_1 field are rotated less and magnetic moments in areas of high B_1 field are rotated more than the nominal pulse nutation angle.

Figure 4.3 compares the thermodynamic equilibrium data directly with the $90°_{+x}$ data from Figures 4.1 and 4.2. The data are displayed from different perspectives to emphasize the distribution of magnetization across the B_1 field. While Figures 4.3a and 4.3c focus on the y and z components of the magnetization as a function of B_1-field strength, Figures 4.3b and 4.3d plot the intensities of the x, y, and z components separately as a function of B_1 nutation frequency, i.e., as a function of ω_1. At thermodynamic equilibrium the net magnetization contains only z components, which are distributed across a wide range of B_1-field strengths. After the $90°_{+x}$ pulse, the net magnetization contains considerable x, y, and z components instead of the ideal result of only y magnetization. Figures 4.3c and 4.3d show that the 90° condition ($M_z = 0$) is only met for a small portion of the sample at a nutation frequency of about 30 kHz, while the majority of the sample is

found at a nutation frequency of about 39 kHz. This majority of the sample experiences a

nutation angle of much more than 90° (i.e., a nutation angle of about 115°-120°).

Figure 4.3. Experimentally derived magnetization vectors obtained a) at thermodynamic equilibrium of the nuclear spins and c) after a nominal 90° hard pulse. Individual x, y, and z components as a function of B_1 nutation frequency are shown b) at thermodynamic equilibrium and d) after a nominal 90° hard pulse.

Similarly, Figure 4.4 shows experimentally derived B_1 and ΔB_0 dependent magnetization vectors at thermodynamic equilibrium and after a nominal $180°_{+x}$ pulse.
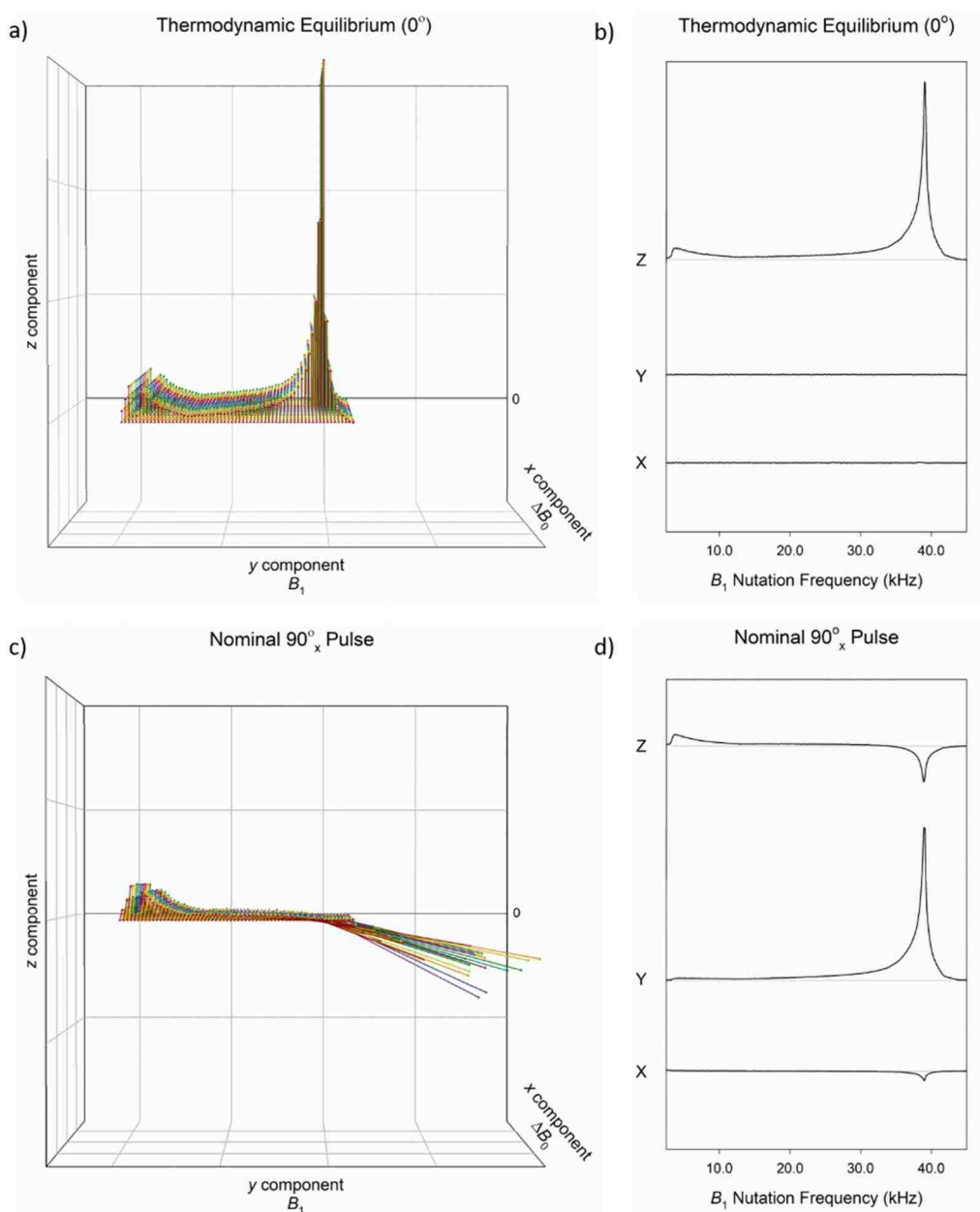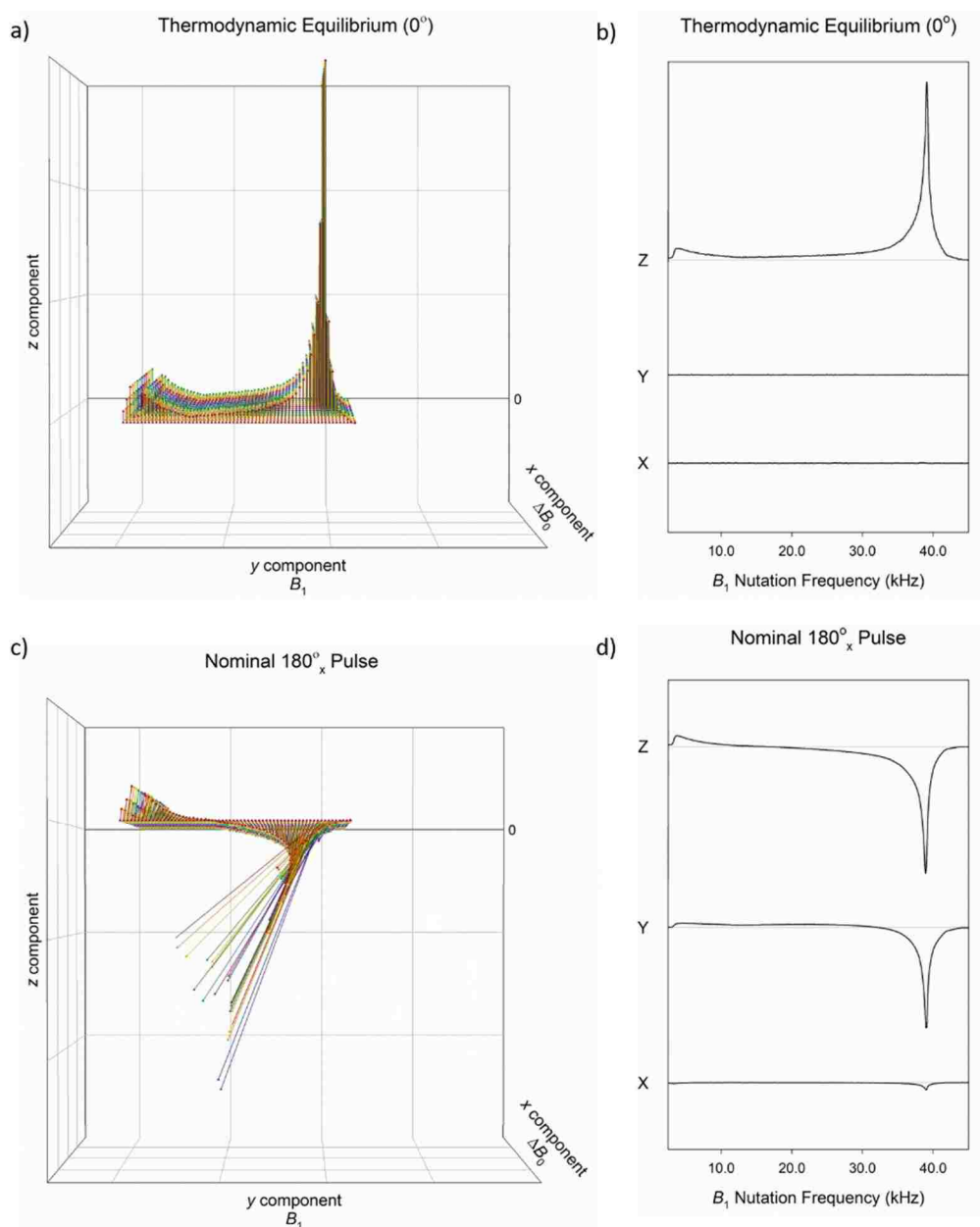

Figure 4.4. Experimentally derived magnetization vectors obtained a) at thermodynamic equilibrium of the nuclear spins and c) after a $180°_{+x}$ hard pulse. Individual x, y, and z components as a function of nutation frequency are shown b) at thermodynamic equilibrium and d) after a $180°_{+x}$ hard pulse.

The magnetization vectors in Figure 4.4a and Figure 4.4c are displayed to emphasize the magnetization distribution across the B_1 field. After the $180°_{+x}$ pulse, the net magnetization contains considerable amounts of x, y, and z components instead of the ideal result of only magnetization in the negative z direction. Figures 4.4c and 4.4d again show that the 180° condition is only met for a small portion of the sample, i.e., at a nutation frequency of about 29 kHz. It is noted that this nutation frequency is different by about 3.5% from the ideal nutation frequency measured earlier for the 90° condition (30 kHz). As a result, a closer investigation of the transmitted RF power during a hard pulse was conducted using the new technique of monitoring the x, y, and z components separately as a function of B_1 field strength.

4.2. PROBE PERFORMACE EXPERIMENTS

The results from the hard-pulse experiments showed the distribution of the magnetization with respect to the B_1 field in a selective, single-channel ^{1}H probe. Similar experiments were conducted using a standard, dual-channel broadband probe to assess differences in the NMR probe performance. The same sample and same parameters were used to conduct the experiments in each probe.

Figure 4.5 shows the profiles of the z component magnetization at thermodynamic equilibrium as a function of nutation frequency obtained from experiments conducted in each probe. The results from the broadband probe are similar to that of the ^{1}H probe, showing that the magnetic moments in the sample are distributed over a wide range of B_1 field strength, and therefore a wide range of nutation frequencies. The results also show that the maximum B_1 field and the corresponding nutation frequency found in the

broadband probe is much lower than in the selective ^{1}H probe. The range of sample with high B_1 field strength (i.e., the range of B_1 field closest to and within the winding of the probe's RF coil) is broader in the broadband probe than it is in the selective ^{1}H probe. This finding may be a result of the different coil geometries in the two probes, where the ^{1}H coil in the broadband probe is further away from the sample to give way for the second-channel broadband coil. It is also larger in size to cover the entire area of the broadband coil for effective decoupling or cross-polarization experiments.

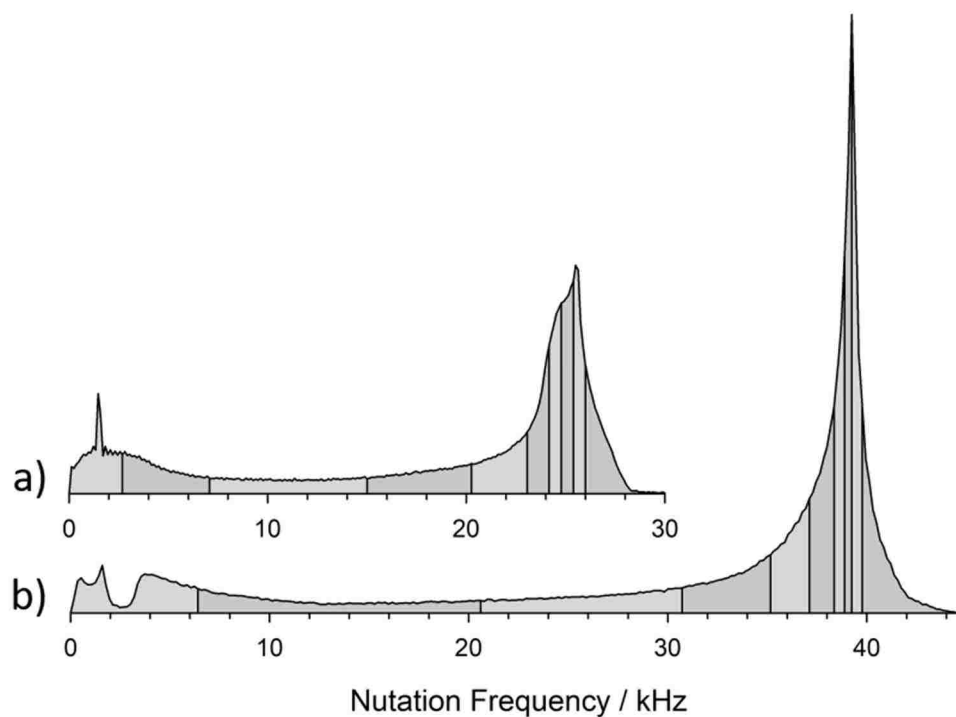Figure 4.5. Profile of the z component of magnetization at thermodynamic equilibrium measured in a) a selective, single-channel ^{1}H probe and b) a standard, dual-channel broadband probe. Segments of each profile indicate 10% of the detected signal.

Nutation-frequency dependent z magnetization profiles (B_1 profiles) for each of the two probes were collected after a single-pulse excitation times ranging from 1 μs to 36 μs

in increments of 1 μs. Each of these profiles was normalized using the z magnetization profile at thermodynamic equilibrium. This process provided curves that are more easily compared in terms of how the resulting profiles at different pulse excitation times relate to each other. For example, points of equal normalized signal intensities are the result of the same pulse nutation angle or, in some cases, the result of the same positive and negative difference in pulse nutation angle from the 180° pulse. Figure 4.6 shows plots of such normalized intensity profiles as a function of nutation frequency for the nominal 30°, 60°, 90°, 120°, 150°, and 180° pulses. The nominal pulse angles have all been derived from the maximum y-component intensity set to 90°. In addition to the normalized intensity profiles, simulated curves are shown in Figure 4.6, which are derived from a weighted least-squares fit of a B_1-dependent cosine function to the experimental data. The B_1-dependent z-component intensities at thermodynamic equilibrium were used as weighting factors, so that the curves are preferentially fitted to the data of strong magnetization.

Although the plots of the normalized z component profiles from the selective ^{1}H probe (Figure 4.6a) and the broadband probe (Figure 4.6b) look similar, it is important to note that the range of nutation frequencies is smaller, and the required pulse lengths are longer, for the broadband probe. This is again attributed to the fact that the broadband probe contains two transmitter/receiver coils, whereas the selective ^{1}H probe contains only one transmitter/receiver coil, which is smaller and positioned closer to the sample. The color-filled points placed on each curve indicate the point in the profile where the actual pulse angle coincides with the nominal pulse angle. Ideally, the actual pulse angles would all occur at the same nutation frequency. For both probes, however, smaller rotation angles are achieved at higher nutation frequencies (higher B_1 field strength), whereas larger

rotation angles are achieved at lower nutation angles (lower B_1 field strength). The discrepancy in the required B_1 to achieve the various pulse angles is significantly larger for the selective ^{1}H probe. The difference is about 6 kHz between the actual 30° and 180° pulses in the ^{1}H probe compared to only about 2.5 kHz between the actual 30° and 180° pulses in the broadband probe.
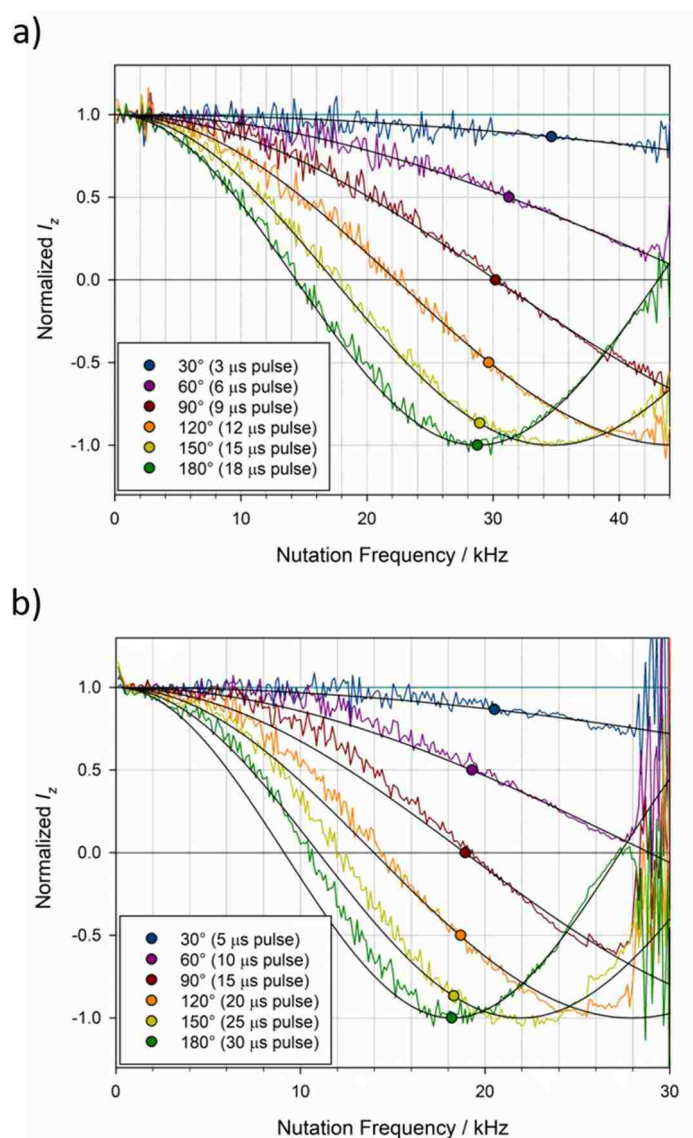

Figure 4.6. Normalized intensities from *z* component profiles measured after a 30°, 60°, 90°, 120°, 150°, and 180° pulse (color lines) and best fit sine curves for each experimental data set (black lines).

The reduction in nutation frequency necessary for larger pulse angles is clearly a shortcoming in NMR transmitter power output and/or NMR probe circuitry. This means that relatively more power is delivered to the probe's resonance circuit as the pulse duration becomes longer. However, in standard preparation of NMR experiments this is overlooked, because pulse angles are considered directly proportional to the pulse duration.

Figure 4.7 shows plots of the average pulse power transmitted in the selective ^{1}H and in the broadband probe as a function of the nominal pulse angle, when the nominal pulse angle is considered proportional to the pulse duration. The experimental data was fitted to an exponential rise-to-maximum curve, indicating that the transmitted pulse power stabilizes over time. The fitted curves indicate that, for the selective ^{1}H probe, only 93.6% of the maximum power output is transmitted by the time the nominal 90° pulse (i.e., the maximum y-intensity pulse) occurs. The power output increases to 98.5% and 99.7% for the nominal 180° and 270° pulses, respectively. This effect is less pronounced for the broadband probe, where 96.4% and 99.4% of the maximum power output are reached by the time the nominal 90° and 180° pulses are achieved, respectively. Based on these results it appears that "gating" the RF pulse does not lead to an instant release of the maximum power from the power amplifier, but instead to a time-dependent, exponential rise to the maximum power output. In addition, the NMR probe's resonance circuit may resist the sudden RF amplitude change when the pulse is applied. The resistance to RF amplitude changes will be more pronounced with higher RLC quality factors (q-factors) of the NMR probe circuit, i.e., with probes that are well tuned and matched to the transmitter frequency and output impedance, respectively [27].
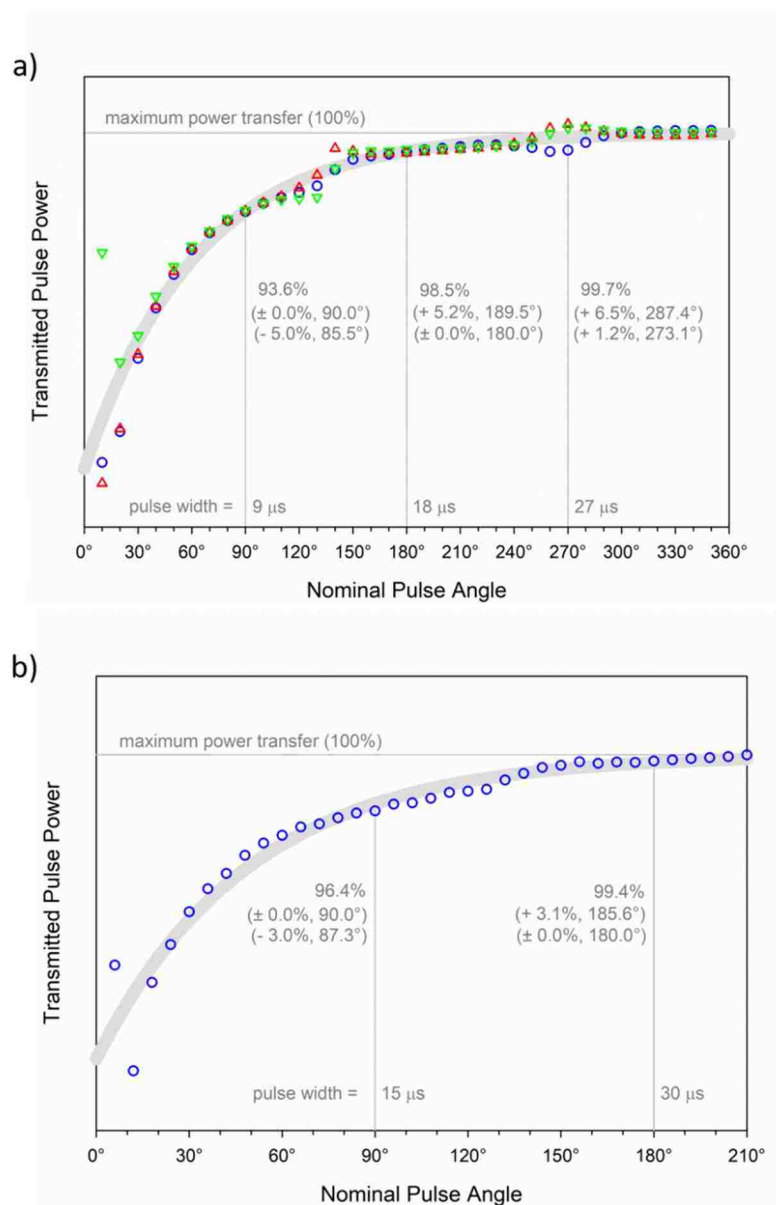
Figure 4.7. Average pulse power transmitted a) in the ^{1}H probe and b) in the broadband probe as a function of the nominal pulse angle, when it is considered proportional to the pulse duration. The data for the selective ^{1}H probe was collected with the transmitter set on resonance (green triangles), at a positive resonance offset of 1 kHz (red triangles), and at a negative resonance offset of 1 kHz (blue circles). For the broadband probe, data were collected with the transmitter set on resonance (blue circles). Grey curves underneath the experimental data curve fits (exponential rise-to-maximum) to the experimental data indicating that the pulse power changes during the pulse. For 9-μs, 18-μs, and 27-μs pulses in the ^{1}H probe, only 93.6%, 98,5%, and 99.7% of the maximum power is transmitted, respectively. For 15-μs and 30-μs pulses in the broadband probe, 96.4% and 99.4% of the maximum power is transmitted, respectively. The numbers in parentheses underneath the percentages of maximum power output show the maladjustments that occur when the pulse power is considered constant during the execution of a pulse.

In Figure 4.7a, the data in parentheses underneath the average power output in percent indicate the deviation from the nominal value when the nominal 90° pulse is used to set the pulse excitation times (first line), and when the nominal 180° pulse is used to set the pulse excitation times (second line). Similar data are provided in Figure 4.7b for the broadband probe. This data shows that the time-dependent variation in the power output leads to a systematic maladjustment of pulse angles even if the B_1-dependence of the nutation angle can be neglected. For example, when the nominal 90° pulse is set at 9 μs in the selective ^{1}H probe, an 18-μs pulse will lead to a 189.5° pulse and a 27-μs pulse to a 287.4° pulse at the same location in the sample. Similarly, at the location where the 18-μs pulse achieves exactly a 180° pulse, the 9-μs pulse will only achieve an 85.5° pulse.

4.3. INVERSION-RECOVERY EXPERIMENTS

To further test the capability of the magnetization tracking protocol, each step in a commonly used multi-pulse NMR sequence, the inversion-recovery (IR) pulse sequence, was monitored. The inversion-recovery sequence is typically used to measure the longitudinal relaxation times, T_1, of a sample [1,28,29]. Figure 4.8 shows the timeline of the inversion-recovery sequence in addition to sketches of the net magnetization throughout the experiment. The sequence begins with a sufficient delay, d1, to ensure that the magnetization of the sample is at thermodynamic equilibrium before beginning or repeating the first pulse of the sequence. A 180°$_{+x}$ pulse is then applied, which rotates the equilibrium net magnetization by 180° about the positive x-axis. Accordingly, the magnetization is inverted resulting in a net magnetization along the negative z-axis. During the relaxation delay, τ, the spin ensemble of the inverted magnetization relaxes back toward

thermodynamic equilibrium given by the Boltzmann equation (Eq. 2). A $90°_{+x}$ observe pulse places the partially recovered magnetization into the *xy*-plane to allow for the measurement of a resonance signal.
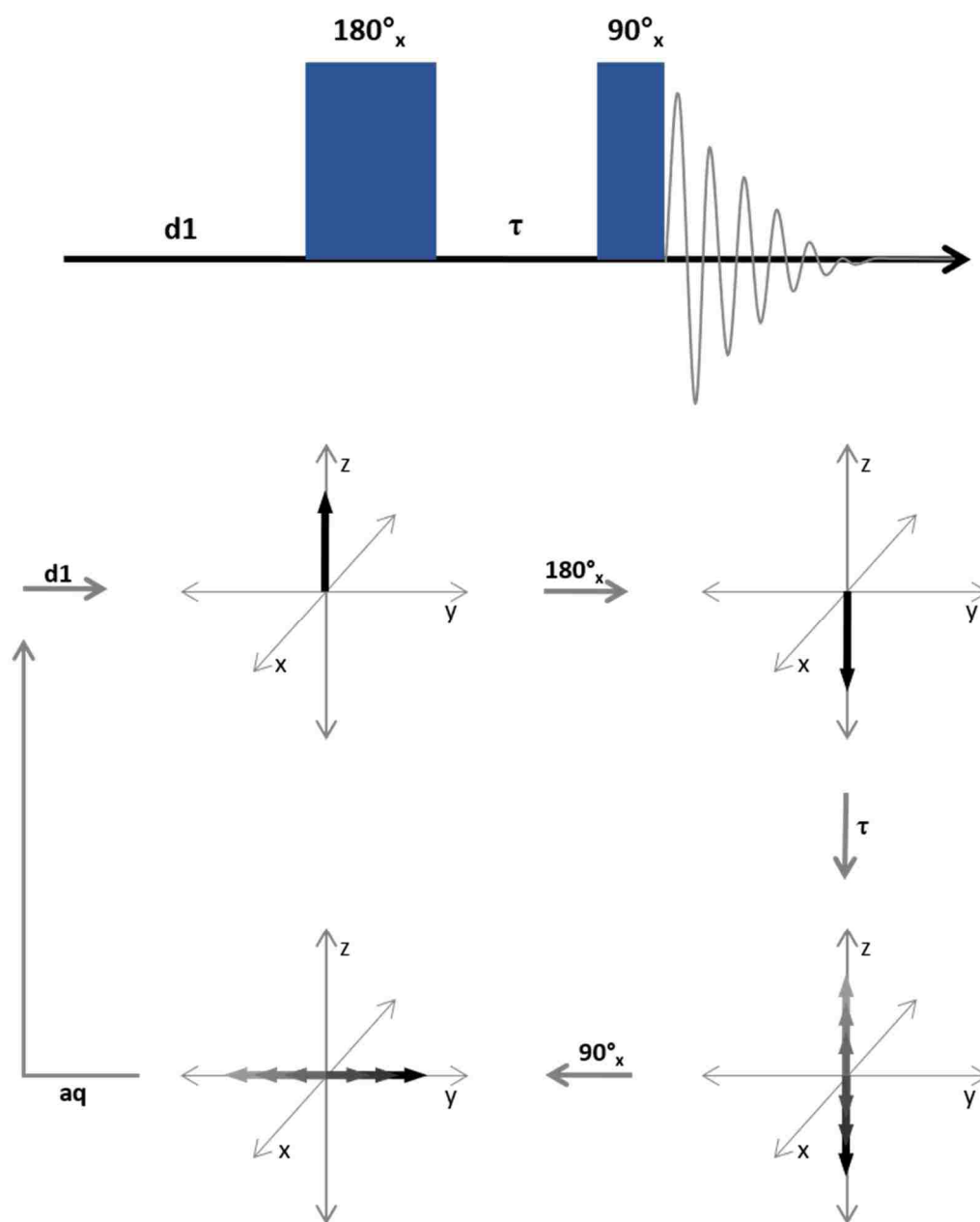

Figure 4.8. Timeline of the inversion-recovery NMR pulse sequence and sketches of the resulting net magnetization throughout the experiment.

Relaxation of the longitudinal component of magnetization is governed by an exponential rise to maximum. The relationship between relaxation delay, τ, and signal intensity, M, is described by:

$$M = M_0 \left(1 - 2e^{-\tau/T_1}\right) \tag{11}$$

where M_0 is the signal intensity at thermodynamic equilibrium, and T_1 is the longitudinal relaxation time constant, which is also termed spin-lattice relaxation time constant or simply T_1 relaxation time. Alternatively,

$$M = M_0 \left(1 - ae^{-\tau/T_1}\right) \tag{12}$$

is used if complete inversion cannot be achieved in the inversion-recovery experiment. The T_1 relaxation time is typically determined by plotting the experimentally derived signal intensities as a function of relaxation delay, τ, and fitting it to Equation 12.

Based on the results of the hard-pulse experiments, it was suspected that the 180° and 90° pulse imperfections could cause significant errors in the measurement of T_1 relaxation times when using the inversion-recovery NMR sequence. Because the nominal 180° profile had already been measured in the hard-pulse experiments (Figures 4.4c and 4.4d), it was not measured again in this investigation. Instead, profiles of the x, y, and z components of the magnetization were obtained after the relaxation delay (Figure 4.9) and after the 90° observe pulse (Figure 4.10).
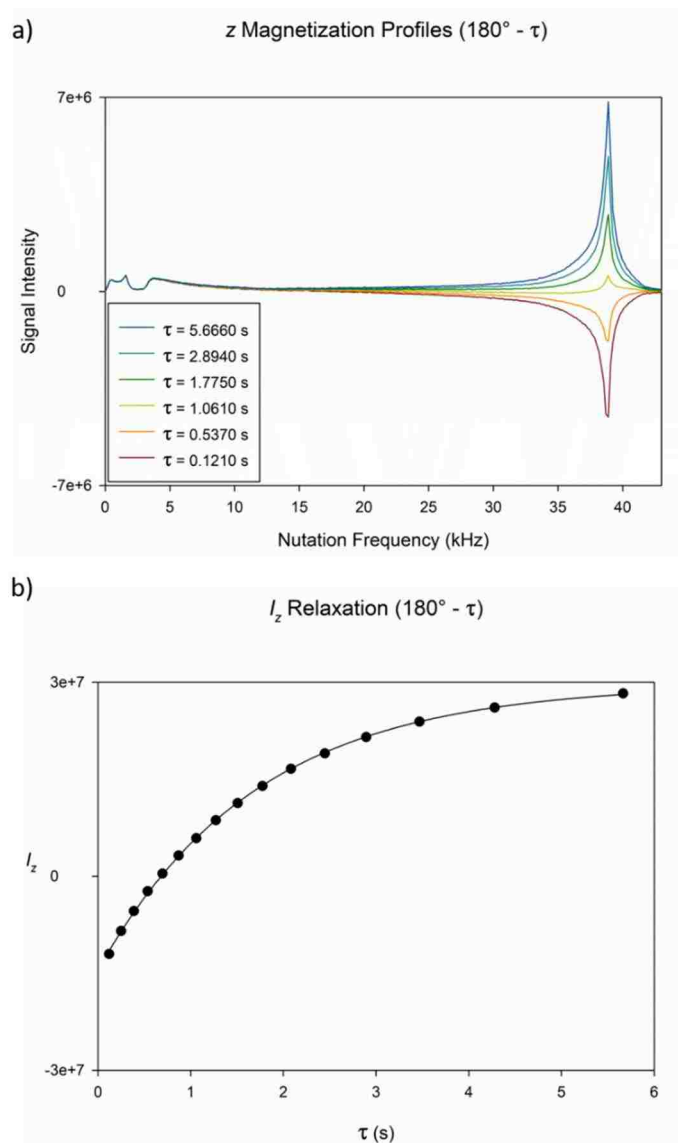
Figure 4.9. Results from the magnetization tracking protocol after the (180° – τ) portion of an inversion-recovery pulse sequence, including a) B_1-dependent profiles of the z component of magnetization after selected τ-delays and b) the total intensity of the z component after each of the τ-delay.

For the first portion of the investigation, the focus was on the z component of the magnetization, because only that portion can be used to quantify the longitudinal relaxation. However, it is important to mention that the nominal 180° pulse results in portions of less than 180° rotation at low B_1 field strengths, portions of more than 180°

rotation at high B_1 field strengths, and an actual 180° nutation at only a specific B_1 field strength. In addition to reduced –z components, significant x and y components are expected at these smaller and larger B_1 field strengths, which could potentially obstruct the accurate measurement of T_1 relaxation times. Figure 4.9a displays some of the recorded z-component profiles after the (180° – τ) portion of the inversion-recovery sequence, where τ represents the relaxation delay between the 180° and the 90° pulse in the sequence. After the shortest relaxation delay, τ, magnetization exposed to the higher B_1 fields is still negative from the 180° inversion pulse, but magnetization at the low B_1 fields, which was only slightly rotated, has already relaxed back close to thermodynamic equilibrium. As the relaxation delay is increased, the magnetization profiles show that the z component of the magnetization steadily relaxes back toward thermodynamic equilibrium. The total intensity for each of the z component profiles as a function of relaxation delay is shown in Figure 4.9b, which shows the expected exponential rise to maximum for a T_1 relaxation measurement.

For the second series of experiments, the focus was put on the y component of magnetization, since that is the component of magnetization recorded to quantify longitudinal relaxation after the observe pulse of the inversion-recovery experiment. It is important to note that not only the nominal 180° pulse but also the nominal 90° observe pulse leads to smaller and larger rotations than expected for a significant portion of the sample. Thus, there are x and z components present that could potentially lead to inaccuracies in T_1 relaxation time measurement. Figure 4.10a displays some of the y-component profiles after the complete inversion-recovery pulse sequence (180° – τ – 90°). Similar to the z-component measurement mentioned above, a short relaxation delay leads

to negative magnetization at high B_1 fields, but instead of negative z magnetizations, it is now negative y magnetizations. As the relaxation delay is increased and the z component of the magnetization steadily relaxes back toward thermodynamic equilibrium, the y component after the 90° observe pulse switches from negative to positive.
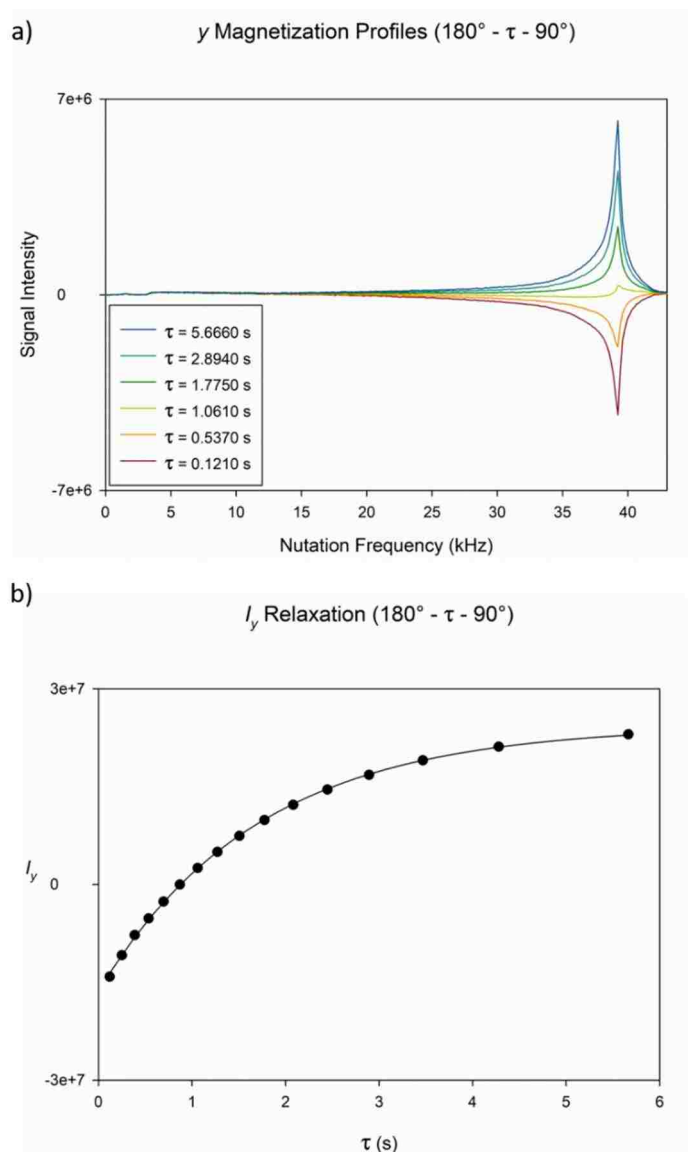

Figure 4.10. Results from the magnetization tracking protocol after the complete inversion-recovery pulse sequence ($180° - \tau - 90°$), including a) several B_1-dependent profiles of the y component of magnetization after selected τ-delays and b) the total intensity of the y component after each of the after selected τ-delays.

The total intensity for each of the y-component profiles is shown in Figure 4.10b as a function of the relaxation delay. Again, the expected exponential rise to maximum is observed. However, close inspection reveals that the y component begins at a slightly larger negative value and does not reach the same maximum compared to the z component that is measured before the 90° pulse.

The T_1 relaxation times are typically extracted from y-component data as a function of delay time which is obtained from a series of inversion-recovery experiments at various relaxation delays. Normally the complete sequence (180° – τ – 90°) is needed because only transverse magnetization (x- or y-magnetization) is observable with NMR spectroscopy. However, utilizing the magnetization tracking protocol, any magnetization components can be monitored, and relaxation times can either be quantified directly from the z component before the 90° observe pulse or from the y component after the 90° observe pulse. Both methods were used to quantify the T_1 relaxation time of water that was dissolved in deuterated water. Trace amounts of copper(II) sulfate ($CuSO_4$) were added to the solution of water in deuterated water to adjust the T_1 relaxation time from about 15 s down to a value of about 1.7 s [30]. The measurements were recorded in a variety of ways, and the results are shown in Figure 4.11. First, the relaxation time was quantified using the total integrated intensity of each profile as a function of delay time, resulting in a relaxation time constant of $T_1 = 1.71$ s from the z-magnetization measurements (180° – τ) and from the y-magnetization measurements (180° – τ – 90°) a value of $T_1 = 1.70$ s. The agreement between the z- and the y-magnetization measurement indicates that imperfections in the 90° observe pulse only slightly impact the inversion-recovery relaxation time measurement.
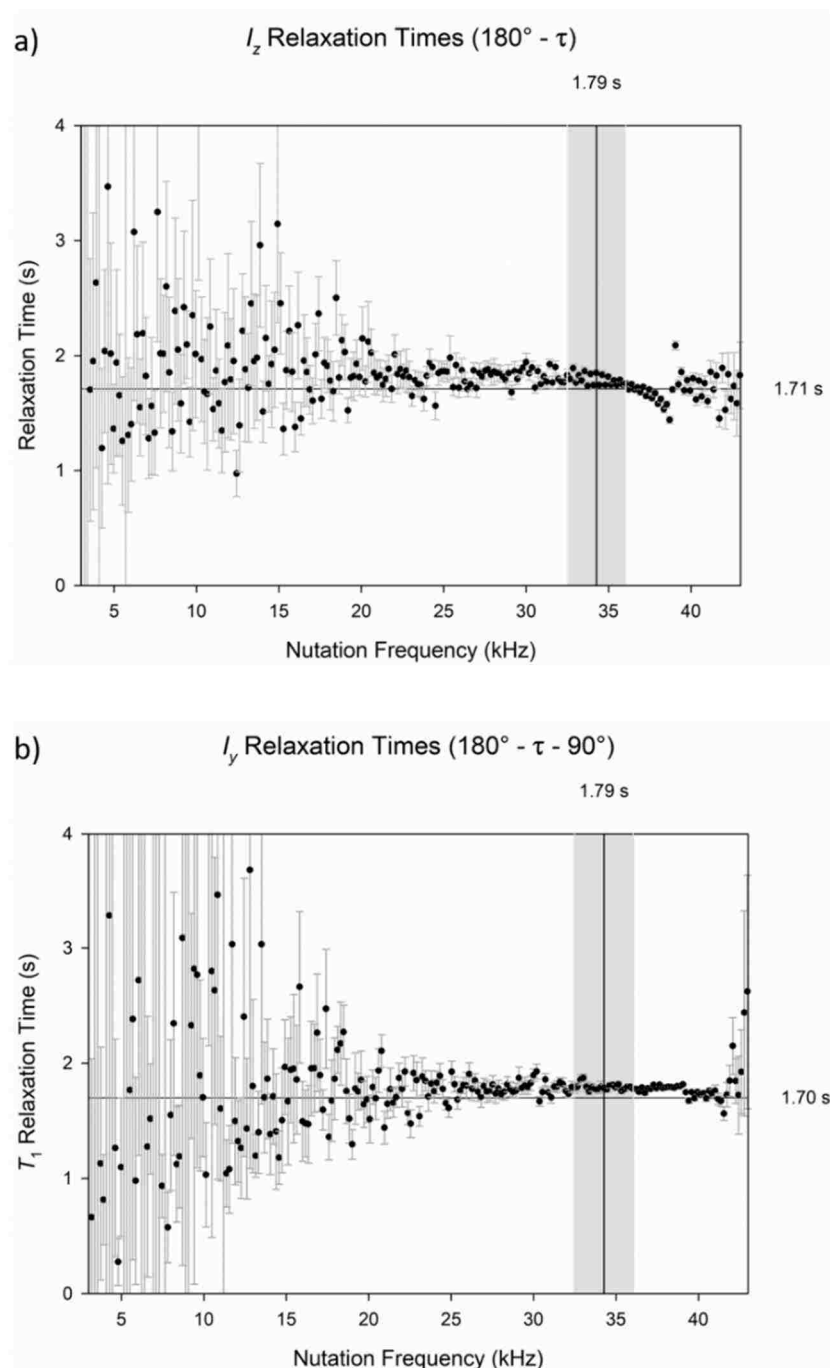
Figure 4.11. T_1 relaxation time measurements a) for each point along the profile of the z component after the $(180° − \tau)$ sequence and b) for each point along the profile of the y component after the complete inversion-recovery pulse sequence $(180° − \tau − 90°)$. The horizontal lines at a) 1.71 s and b) 1.70 s indicate the T_1 relaxation values obtained from the total z- and y-component signal intensities, respectively, as a function of relaxation delay. The vertical, gray-shaded areas indicate the range of B_1 field strength that fall within $\pm 5\%$ of the actual 180° pulse. The T_1 relaxation time values obtained from data within these areas are displayed above the shaded areas.

T_1 relaxation times were also evaluated individually from each data point in the B_1-dependent z and y profiles, resulting in T_1 relaxation times as a function of nutation frequency data. The error bars shown with the T_1 data indicate that the small portions of magnetization at low B_1 fields and their minimal excitation by the nominal 180° pulse do not provide reliable data for relaxation measurements. On the contrary, the large portions of magnetization at high B_1 fields provide relaxation time values that are similar to the value obtained from the total intensity data. Lastly, the T_1 relaxation time constant was evaluated based only on the portion of magnetization that experiences a B_1 field strength within ±5% of the actual 180° pulse. The result of this analysis was the same for the z-component and y-component measurements ($T_1 = 1.79$ s), but significantly different (+5%) from the value obtained from the total intensity data (1.71 s and 1.70 s, respectively). As a consequence, it is concluded that T_1 relaxation time constants derived from standard inversion-recovery experiments can only be obtained within an error margin of ±5%.

4.4. EXCEPT SOLVENT-SUPPRESSION EXPERIMENTS

Experiments were also conducted with the newly developed presaturation-based solvent-signal suppression sequence EXCEPT (EXponentially Converging Eradication Pulse Train) [31]. This sequence uses a train of frequency-selective, adiabatic inversion pulses (hyperbolic secant, or short, sech pulses) spaced out with exponentially decreasing interpulse delays [32, 33]. The progressively decreasing delays d_i, where i denotes the delay following the ith pulse, were calculated according to the recursive formula

$$d_i = d_n(n - i + 1)^x \qquad (13)$$

where x is the exponent of convergence and n is the number of inversion pulses in the sequence, i.e., $n = 16$ for EXCEPT-16. The delays (Table 4.1) were computer optimized to saturate magnetization over a wide range of T_1 relaxation.

Table 4.1. Interpulse delays optimized for the suppression of longitudinal magnetization with relaxation time constants, T_1, within the range of $1 - 10$ s for the solvent suppression sequences EXCEPT-12, EXCEPT-16, EXCEPT-20, and EXCEPT-24, where the number indicates the number of progressively decreasing interpulse delays in the EXCEPT sequence.

Delay	EXCEPT-12	EXCEPT-16	EXCEPT-20	EXCEPT-24
d_i	x = 2.95	x = 3.65	x = 3.89	x = 4.01
d_1	17.12268	18.88342	20.47159	21.28725
d_2	13.24374	14.92077	16.76581	17.94438
d_3	9.995602	11.59956	13.58337	15.01201
d_4	7.323546	8.850851	10.87336	12.45500
d_5	5.172570	6.608794	8.587350	10.23979
d_6	3.487383	4.810769	6.679394	8.334415
d_7	2.212361	3.397455	5.106032	6.708471
d_8	1.291496	2.312937	3.826320	5.333143
d_9	0.668329	1.504821	2.801848	4.181196
d_{10}	0.285851	0.92437	1.996757	3.226971
d_{11}	0.086352	0.526655	1.377762	2.446384
d_{12}	0.011157	0.270743	0.914176	1.816926
d_{13}	---	0.119919	0.577939	1.317663
d_{14}	---	0.041969	0.343642	0.929231
d_{15}	---	0.009556	0.188568	0.633835
d_{16}	---	0.000762	0.092725	0.415249
d_{17}	---	---	0.038896	0.258813
d_{18}	---	---	0.012691	0.151429
d_{19}	---	---	0.002618	0.081562
d_{20}	---	---	0.000176	0.039234
d_{21}	---	---	---	0.01602
d_{22}	---	---	---	0.005049
d_{23}	---	---	---	0.000992
d_{24}	---	---	---	0.000061

The effect of the EXCEPT solvent suppression sequence is demonstrated in Figure 4.12, which shows a spectrum of an aqueous solution obtained from a hydrothermal biomass-to-fuel (BTF) conversion experiment both with and without EXCEPT solvent suppression. In this experiment, glucose was used as a model substrate for carbohydrate-based biomass, such as starch or cellulose, and reacted at 150°C for nine hours in a sealed pressure vessel.
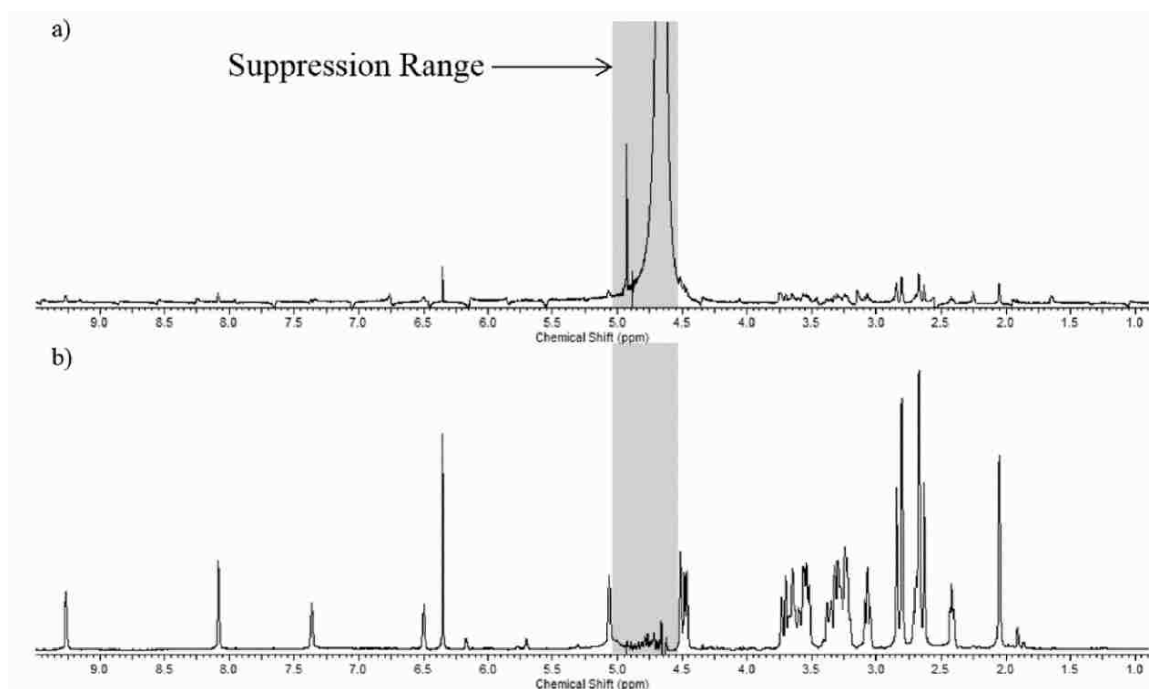

Figure 4.12. ^{1}H-NMR spectra from sample consisting of 600 μL of room temperature solution taken from the reaction of 0.2 M D-glucose in citric acid buffer in a standard glass pressure vessel for 9 hours at 150°C. 150 μL of 99.5% D_2O was added for a field-frequency lock. a) Spectrum obtained with 90° pulse (11 μs) and 16 scans. b) Spectrum obtained with an EXCEPT-16 solvent-suppression pulse sequence under an identical set of acquisition parameters.

As shown in Figure 4.12a, without solvent suppression the strong water signal impedes the analysis of the dilute BTF products; the analog-to-digital conversion cannot

accurately represent the weak signals that are substantially distorted in the baseline as well as lost in the noise. Figure 4.12b shows the superior water-signal suppression that is achieved with EXCEPT along with a flat baseline and excellent signal phasing. From the NMR spectra with EXCEPT solvent suppression, several reaction product such as 5-hydroxymethylfurfural (5-HMF), levulinic acid (4-oxopentanoic acid), lactic acid (2-hydroxypropanoic acid), acetic acid (ethanoic acid), and sometimes even methane gas have been identified as products of the hydrothermal degradation.

Although the solvent suppression achieved by the EXCEPT sequence appears to be sufficient for most samples, the new magnetization tracking protocol was used to assess the cause of the remaining solvent magnetization in an attempt to further optimize the EXCEPT sequence. Figure 4.13 shows B_1-field dependent y-magnetization profiles derived from data collected after a single $90°_{+x}$ pulse and after EXCEPT-20 followed by a $90°_{+x}$ pulse for a sample of water in deuterated water. EXCEPT-20 significantly suppresses the water signal, however, some magnetization remains at low and high nutation frequencies.
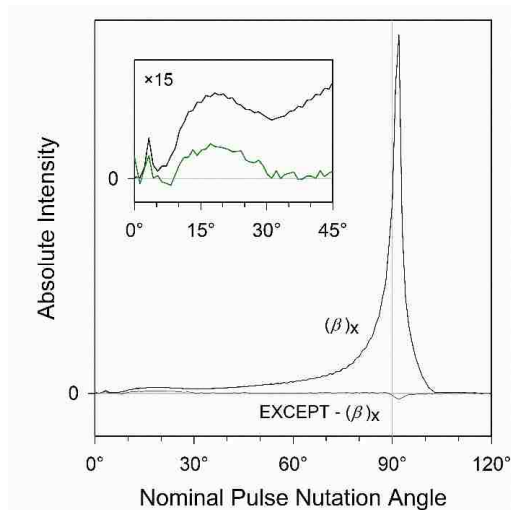
Figure 4.13. B_1-field dependent y-magnetization profiles after a 90° pulse and after EXCEPT-20 followed by a 90° pulse.

A compensation strategy that is based on the linearity condition for small-angle excitation [34] was combined with the EXCEPT sequence to target the residual solvent signal from spins that experience very small flip angles. In this strategy, three scans with a nominal $90°_{+x}$ pulse, or $(\beta)_{+x}$ pulse, are added together with one scan of a nominal $270°_{-x}$ pulse, or $(3\beta)_{-x}$ pulse, while the receiver phase was kept at the y-axis throughout all four scans. For B_1 fields close to the field strengths of the true $90°$ pulse, signal intensities from the three $(\beta)_{+x}$ pulse experiments and the $(3\beta)_{-x}$ pulse experiment should add constructively, while signal intensities from areas of very low field strengths should cancel. Figure 4.14 shows the results of applying this strategy to the EXCEPT solvent-suppression experiment, adding three scans of the EXCEPT sequence each followed by a $(\beta)_{+x}$ observation pulse to one scan of EXCEPT followed by a $(3\beta)_{-x}$ observation pulse.
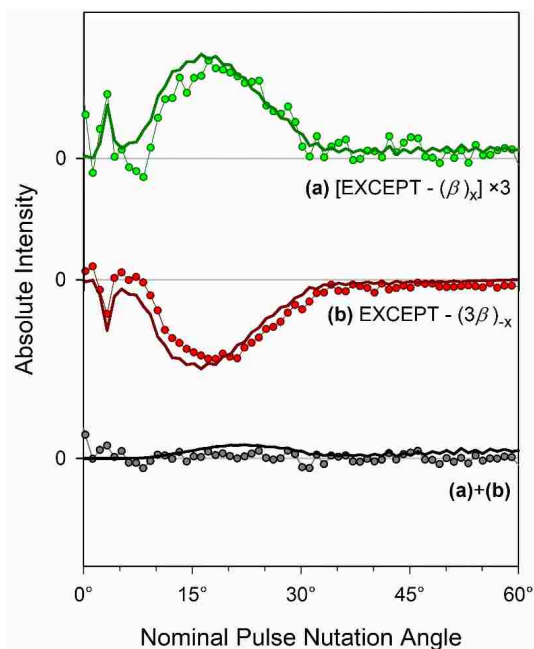
Figure 4.14. B_1-field dependent y-magnetization profiles comparing the experimental results (plotted as data points connected with a thin line) and calculated theoretical results (plotted as thick lines) of the EXCEPT paired with the small-angle flip compensation strategy.

Figure 4.14 displays a breakdown of experimental results, including three times the EXCEPT - $(\beta)_{+x}$ sequence (green data points, Figure 4.14a) and the EXCEPT - $(3\beta)_{-x}$ sequence (red data points, Figure 4.14b). The addition of the intensities from Figure 4.14a and 4.14b leads to complete eradication of the remaining intensity at low B_1 field strengths (dark gray data points, Figure 4.14c). In addition to the experimental data, theoretical intensities (solid lines in Figure 4.14) are shown from an independently recorded z-magnetization profile derived immediately after the EXCEPT sequence. As predicted by the theory and seen in the experimental data, the compensation strategy for small-angle excitations nearly eliminates all remaining signal intensity at low nutation frequencies (i.e., weak B_1 fields).

5. CONCLUSION

The new protocol for monitoring x, y, and z magnetization components independently is a powerful technique for exposing hardware deficiencies and performance limits of NMR probes and spectrometers. In addition, the protocol can be used to experimentally assess specifically designed pulses and pulse sequences to identify shortcomings and potential artifacts. For instance, a nominal 90° pulse which is optimized for obtaining the maximum signal intensity (maximum transverse magnetization and minimum longitudinal magnetization) actually contains a wide distribution of remaining longitudinal magnetization. While the net z magnetization may be zero, large amounts of longitudinal magnetization remain because of B_1 field inhomogeneities across the sample volume. Utilizing such 90° hard pulses in more complex pulse sequences may result in substantial artifacts due to remaining longitudinal magnetization being reintroduced into the transverse plane. Furthermore, the deficiencies in homogeneous pulse excitation because of B_1 inhomogeneities across the sample volume not only apply to 90° pulses but also to other pulses, as seen in all other nominal pulses that have been studied using this protocol. Although this general effect is consistent for all pulse angles, the actual profile with respect to B_1 field strength is dependent on the probe electronics. Differences in the probe electronics can include different coil arrangements, such as a single-coil versus dual-coil probe, as well as differences in the coil quality. The magnetization tracking protocol introduced here can be used as a tool to better understand a given probe's performance, thus providing an opportunity to target a particular probe's deficiencies.

The application of this new protocol to the study of individual pulses and general probe performance is only the beginning of its intended purpose. Although the experimental time would increase with increased pulse sequence complexity, this protocol can be used to track the individual magnetization components of the net magnetization throughout pulse sequences. Investigations into the standard inversion-recovery pulse sequence for measuring T_1 relaxation time revealed that, although this is an accepted method for measuring T_1 relaxation time, it may yield relaxation times that are significantly different than that of magnetization that undergoes a true inversion. In this study, a deviation of up to 5% was measured for the relaxation time of water in deuterated water. Measurements of the individual magnetization components after application of the newly developed presaturation solvent-suppression sequence EXCEPT showed that insufficient solvent-signal suppression occurs particularly in regions that are exposed to very low and very high B_1 field strength. This result helped directing the research focus specifically toward improving the solvent suppression at very low B_1 field strengths and to find a solution for that area.

6. FUTURE WORK

The newly developed protocol has provided useful information about the general insufficiencies in hard pulses, probes, and some specific pulse sequences, but its work is far from complete. One important direction for future experiments will focus finding ways to use the knowledge gained about a particular probes performance to make general adjustments that can improve the overall performance regardless of the pulse sequence being used. In addition, investigations will be conducted on soft pulses, shaped pulses, and composite pulses to compare their behavior to that of hard pulses. Further studies will also be conducted on the EXCEPT solvent-suppression sequence, but with a focus on how it compares to other solvent suppression sequences. This will serve to better understand whether there are benefits to using one solvent suppression sequence over another.

Lastly, although this protocol shows great potential, there still may be room for improvement of the x- and y-component measurements. Since the rotated x magnetization remains along the x-axis during both scans for the y measurement and the rotated y magnetization remains along the y-axis during both scans for the x measurement, there is a chance of interference of the remaining x and y magnetization with the measurement of the y- and x-component measurements. Ideally, the remaining magnetization perpendicular to the receiver is not "seen" by the receiver, but to be certain that it is not impacting the x and y measurements an alternative strategy can be tested. The same strategy that was used for the z measurement could be used for the x and y measurements if these magnetization components were first rotated to the z-axis, applying a $90°_{+x}$ first for the y component and a $90°_{-y}$ first for the x component.
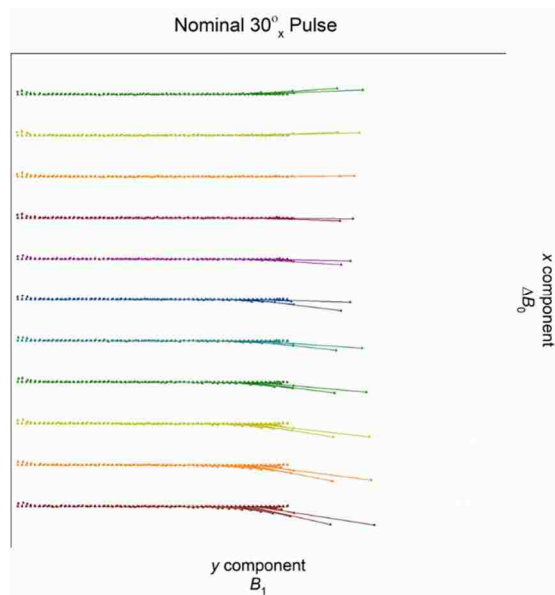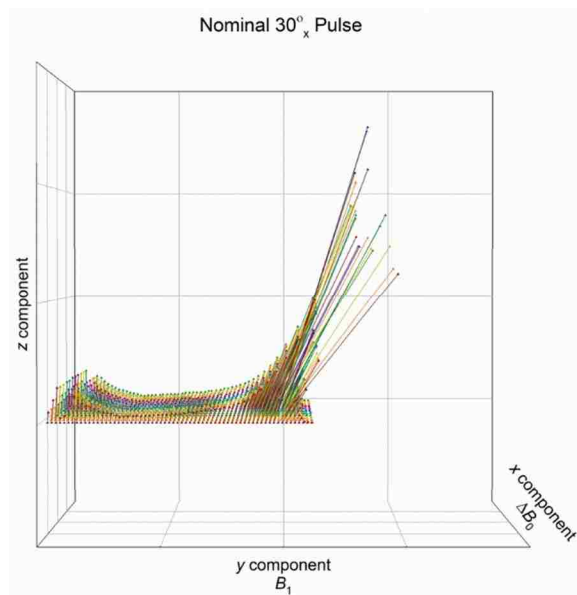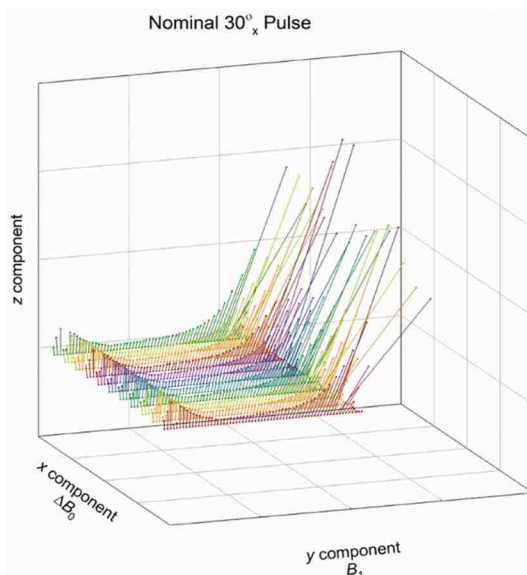
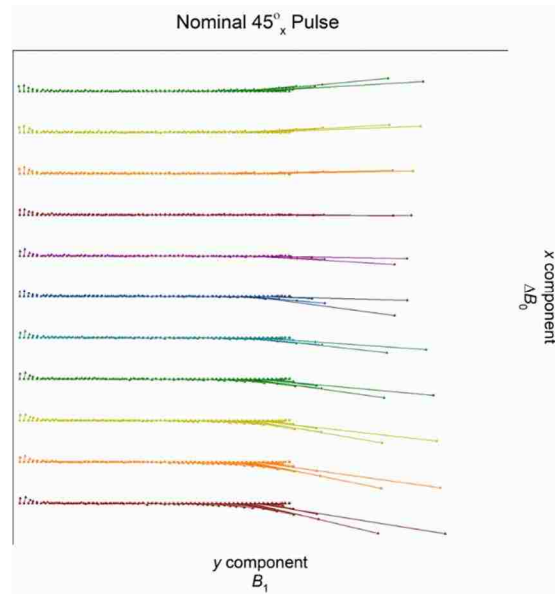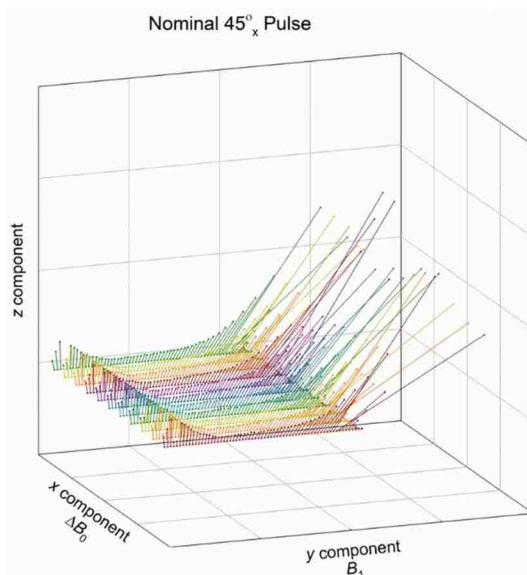**APPENDIX A.**

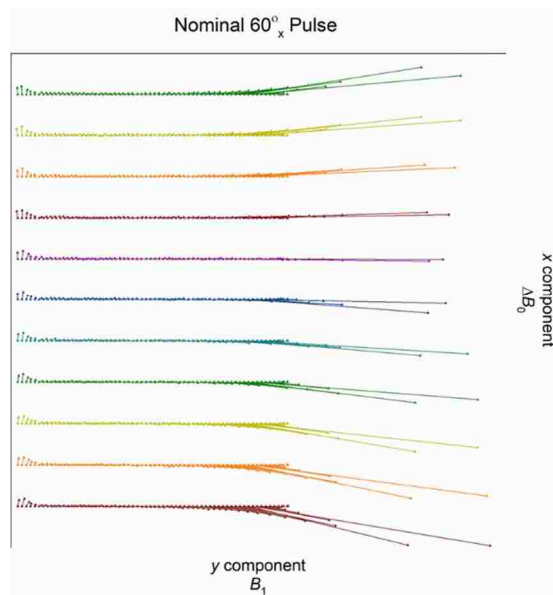**ADDITIONAL PLOTS**

Thermodynamic Equilibrium (0°)
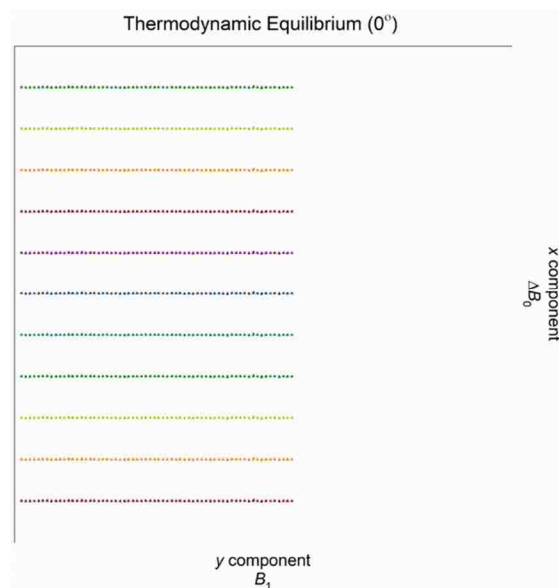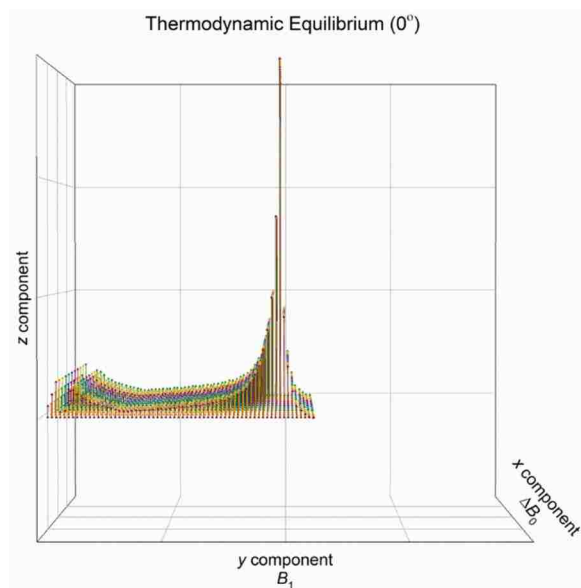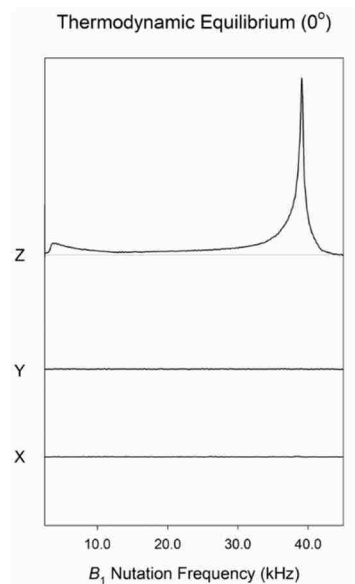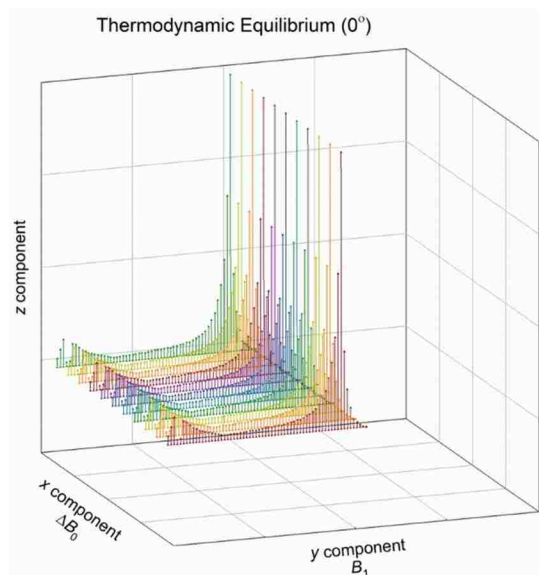
Nominal 15° Pulse

Nominal 15°ₓ Pulse

Nominal 15°ₓ Pulse

Nominal 15°ₓ Pulse
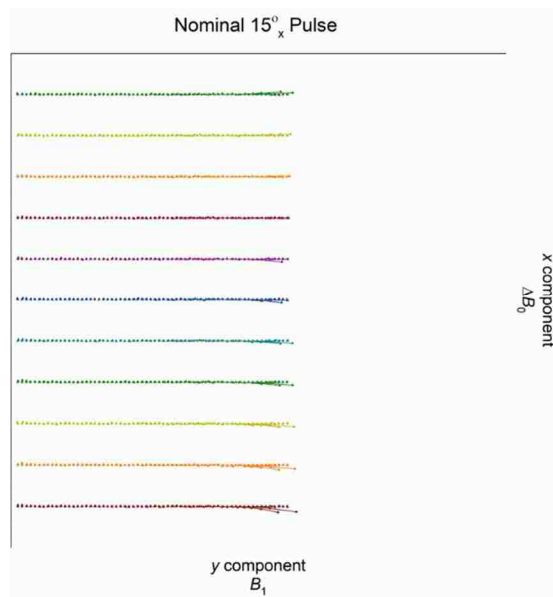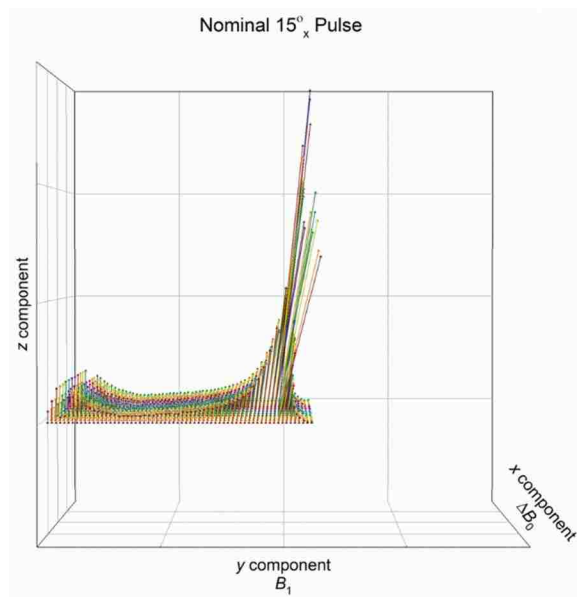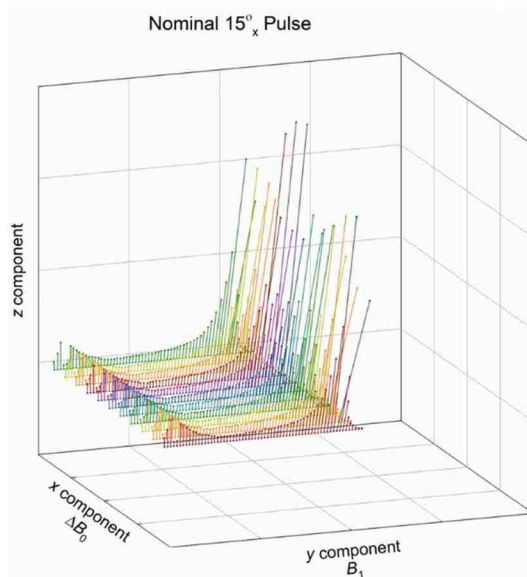
Nominal 30° Pulse

Nominal 30°$_x$ Pulse

Nominal 30°$_x$ Pulse

Nominal 30°$_x$ Pulse

Nominal 45° Pulse

Nominal 45°ₓ Pulse

Nominal 45°ₓ Pulse

Nominal 45°ₓ Pulse
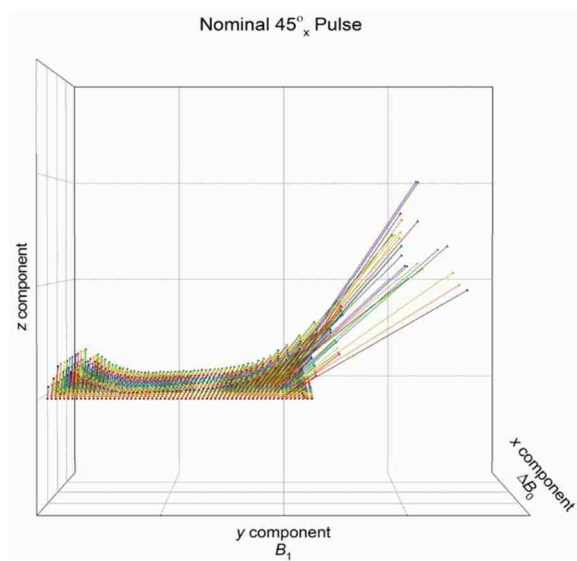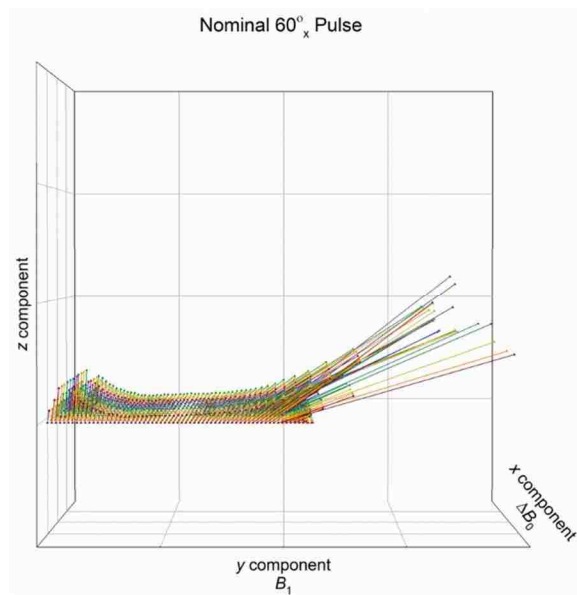
Nominal 60° Pulse

Nominal 75° Pulse

Nominal 75°ₓ Pulse
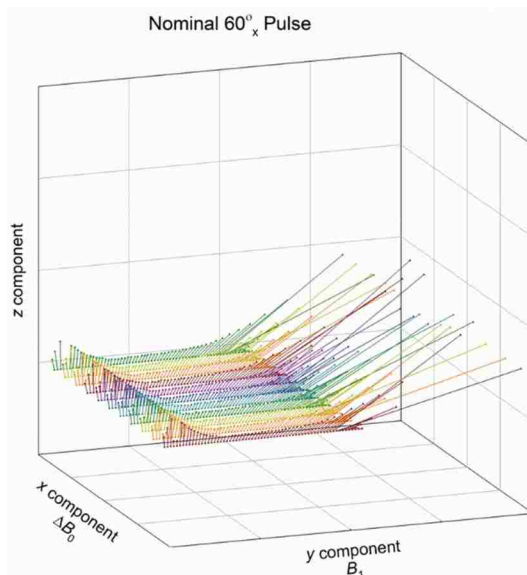

Nominal 75°ₓ Pulse

Nominal 75°ₓ Pulse
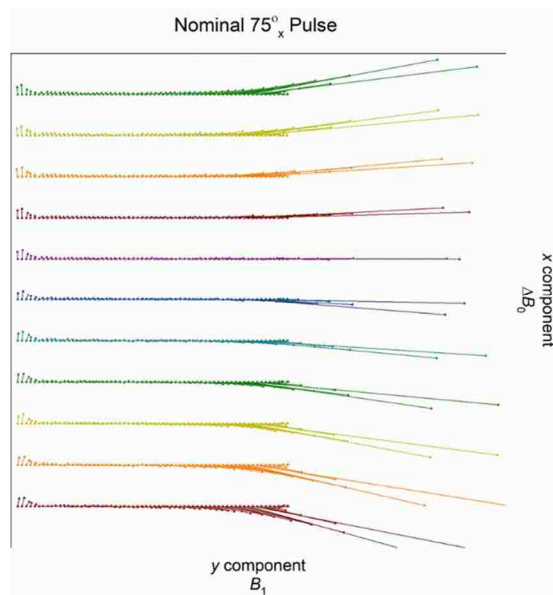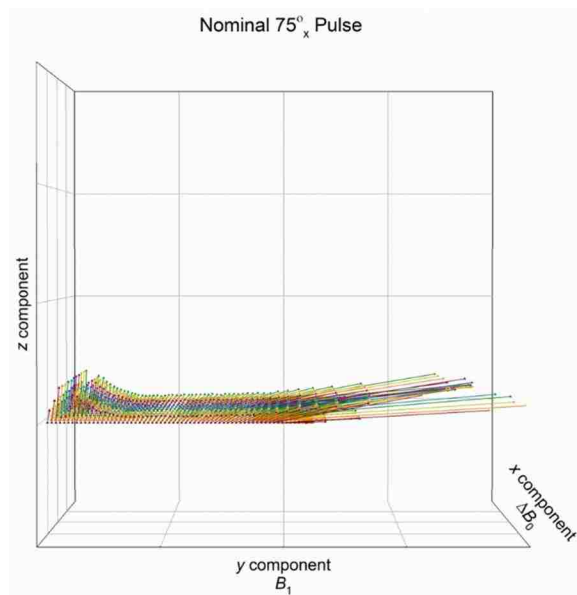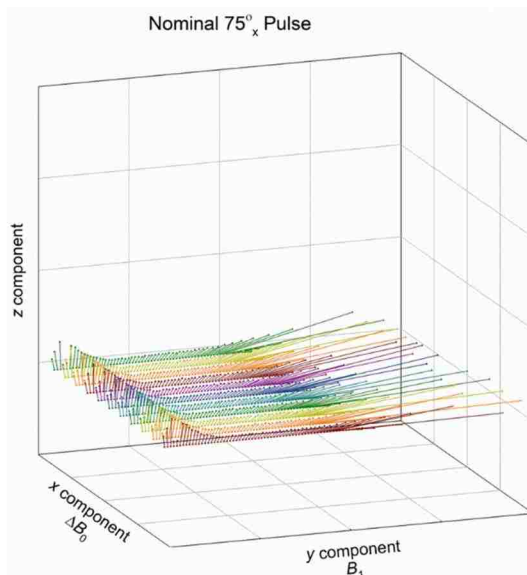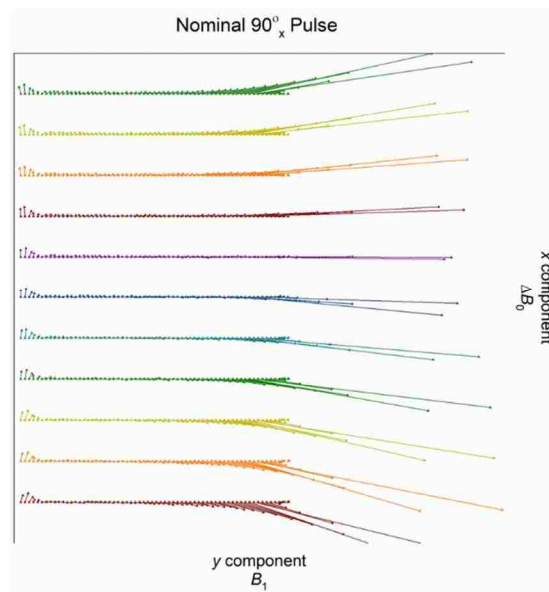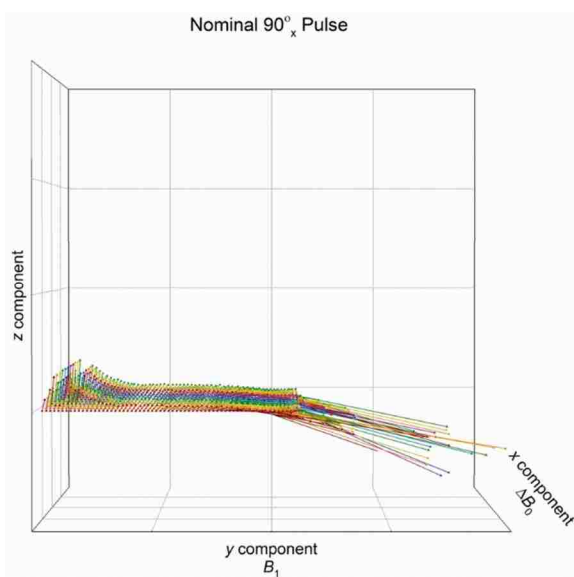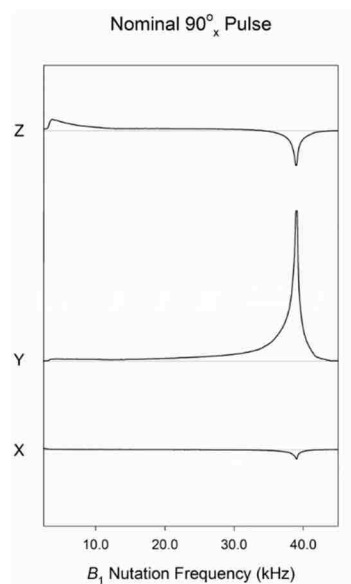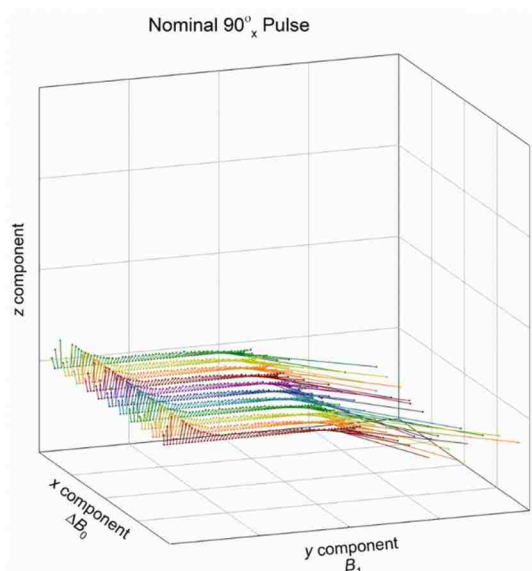
Nominal 90° Pulse

Nominal 180° Pulse
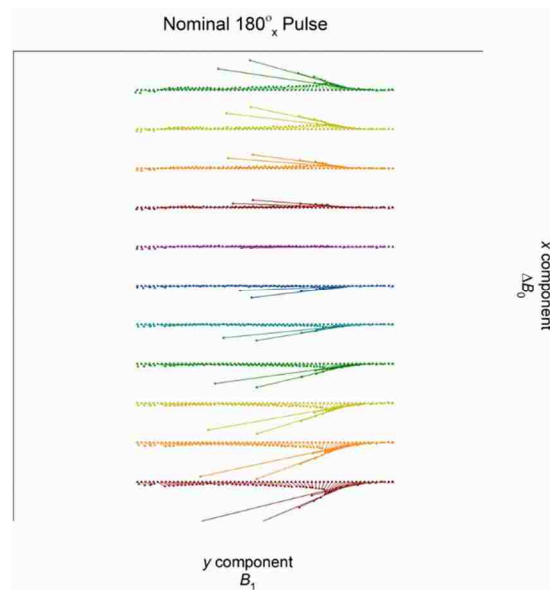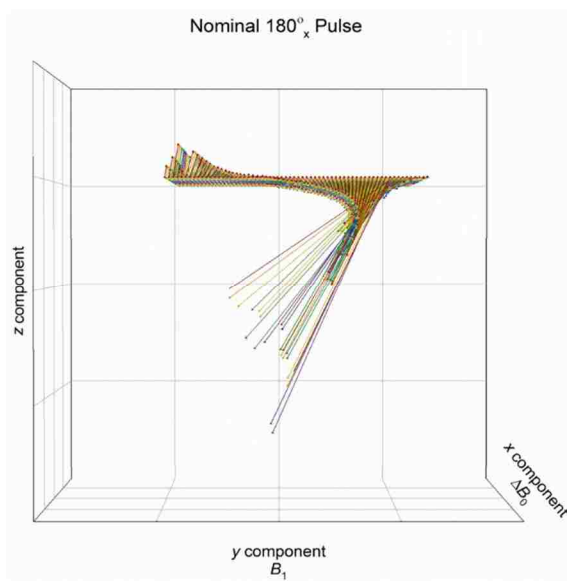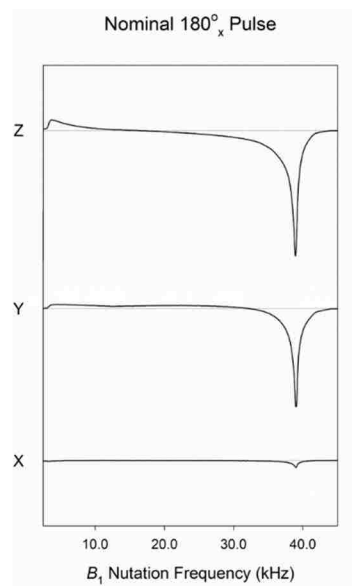
Nominal 270° Pulse

Nominal 270°ₓ Pulse

Nominal 90°ₓ Pulse

Nominal 270°ₓ Pulse

Inversion Recovery Analysis (180° – τ)

IR *x* Profiles

IR *y* Profiles

IR *z* Profiles

Inversion Recovery Analysis (180° – τ – 90°)

T1 IR *x* Profiles

T1 IR *y* Profiles

T1 IR *z* Profiles
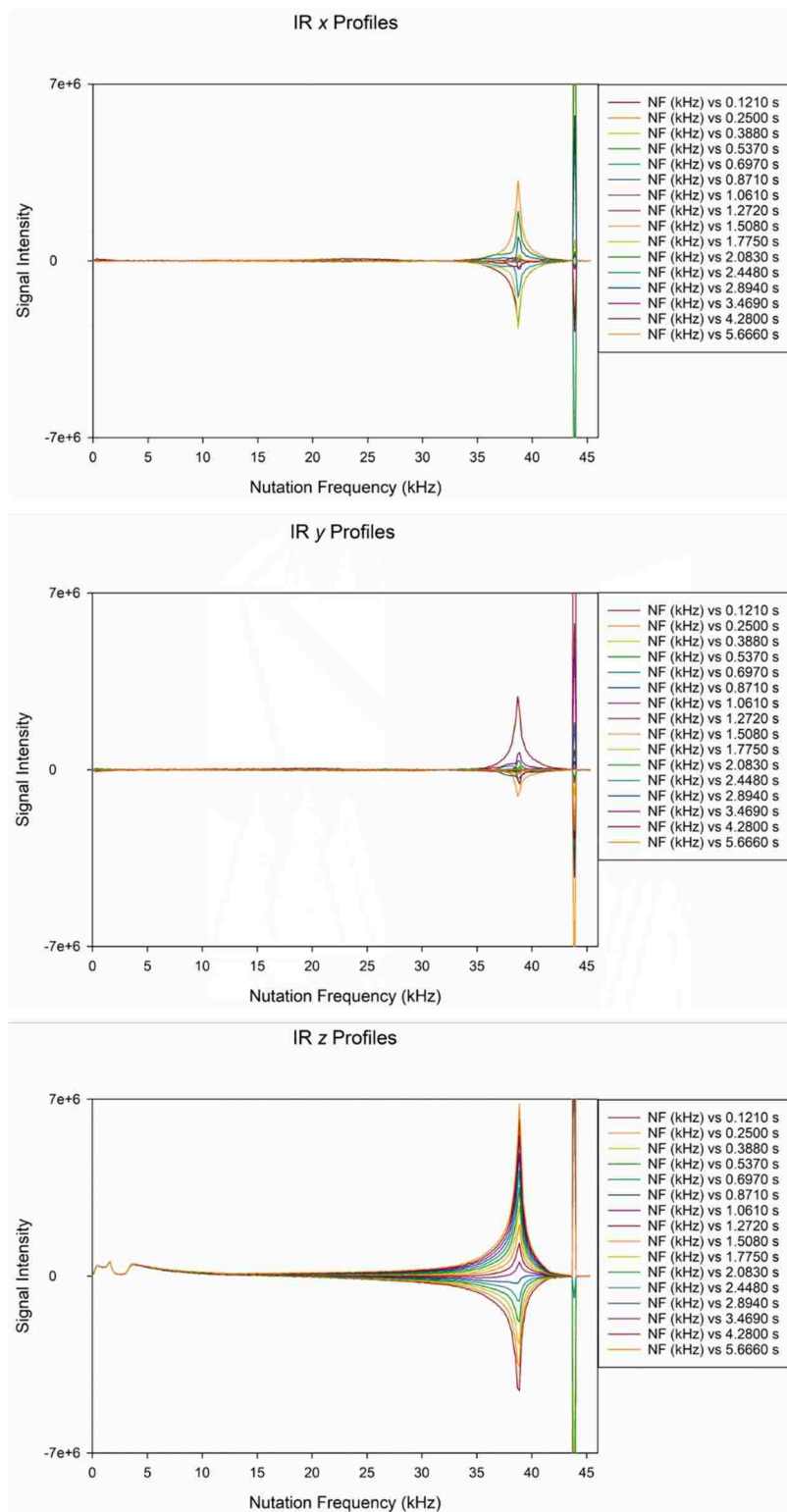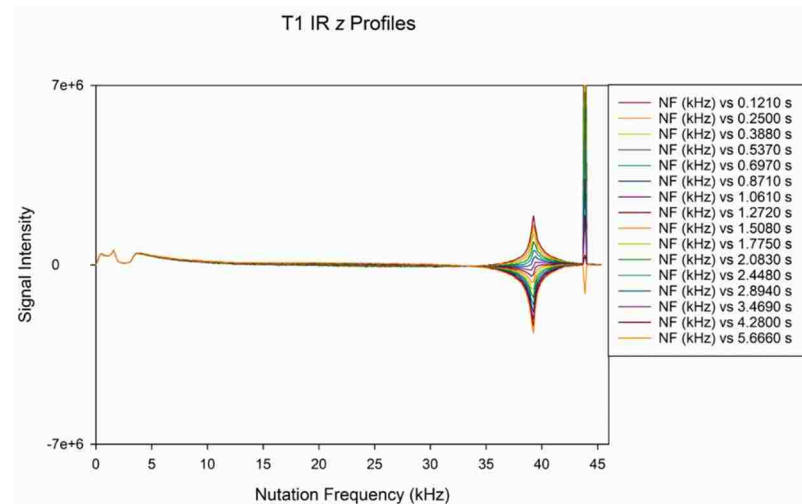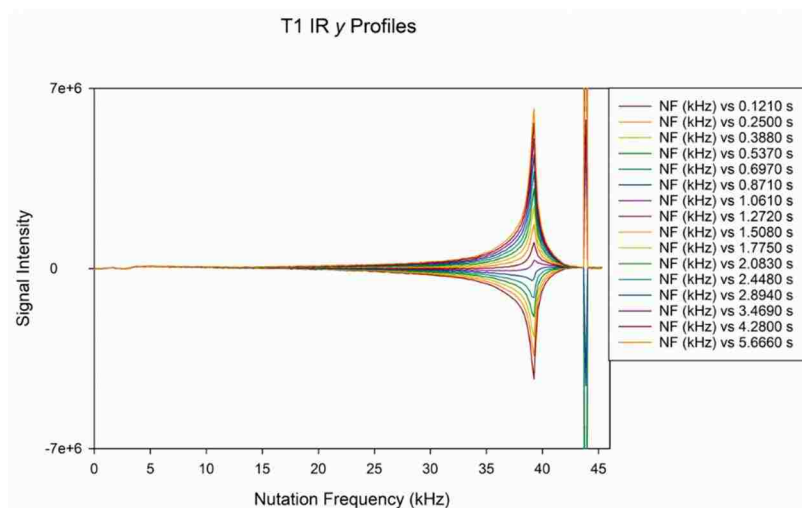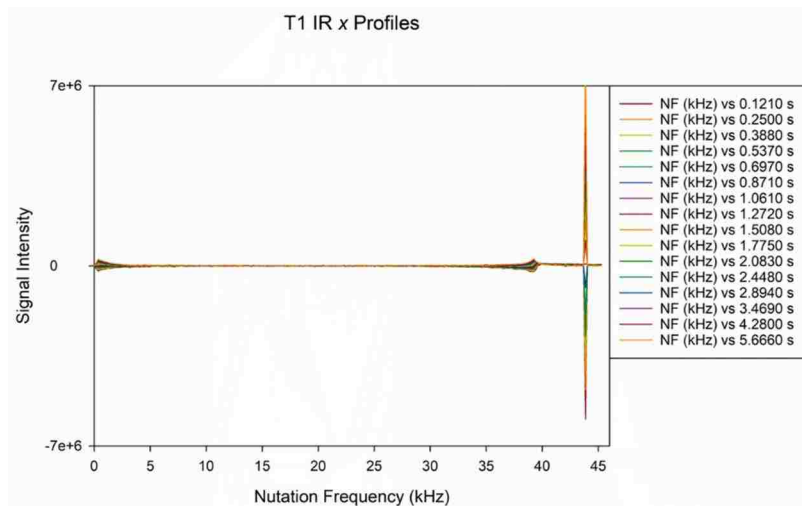
APPENDIX B.

PULSE PROGRAMS

Pulse sequence for *x* nutation imaging with RIPT after a single pulse (zz_ript_x_1D)

```
define pulse px;
define loopcounter tdov;

"px=1u"                          ; dwell-pulse, "pulse" for receiving one data point
"tdov=td"                        ; loop increment for RIPT sequence
"d11=30ms"

      100u pl1:f1                 ; set power level for F1, receiver
1     ze

start,  d1 reset:f2 reset:f1      ; F1 and F2 initialization

      de1 fq=cnst1:f2 fq=cnst1:f1 ; set resonance offset for monitored pulse
      de1 pl3:f2                  ; set power level for F2, transmitter, monitored pulse
      (p3 ph3):f2                 ; monitored pulse (or replace w/ a portion or entire sequence)

      de1 fq=0:f2 fq=0:f1         ; on resonance
      de2 adc ph31 syrec pl2:f2   ; open receiver and start digitizer
      de ph30:r

ifg,    d3                        ; nutation image (Interferogramm)
      px:x                        ; receive one data point
      3u:e
      (p1 ph1):f2 :e              ; RIPT pulse
lo to ifg times tdov

      10u
      rcyc=start
      d11 wr #0
exit

; ------- Phase program --------
ph3  = 0 0 2 2 1 1 3 3            ; phase for monitored pulse
ph2  = 0 2 3 1                    ; phase for EXCEPT monitored pulse
ph1  = 1 3 3 1 2 0 0 2            ; phase for RIPT pulse
ph30 = 1 1 3 3 2 2 0 0            ; receiver phase
ph31 = 0

                                 ;d1 : relaxation delay (z.B. 5xT1)
                                 ;d3 : delay between RIPT pulses
                                 ;p1 : RIPT pulse length (dpw)
                                 ;p2 : monitored pulse length
                                 ;td1: number of interferrograms (set in eda)
                                 ;TD : number of data points in the interferrogram
                                 ;NS : number of scans (ns = 2*n)
                                 ;cnst1 : resonance offset for monitored pulse
```
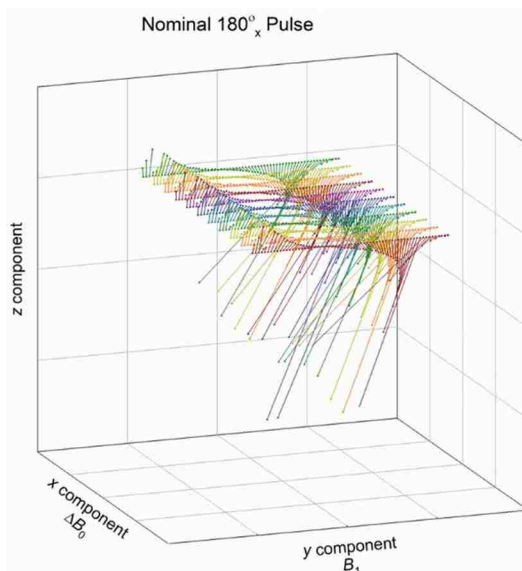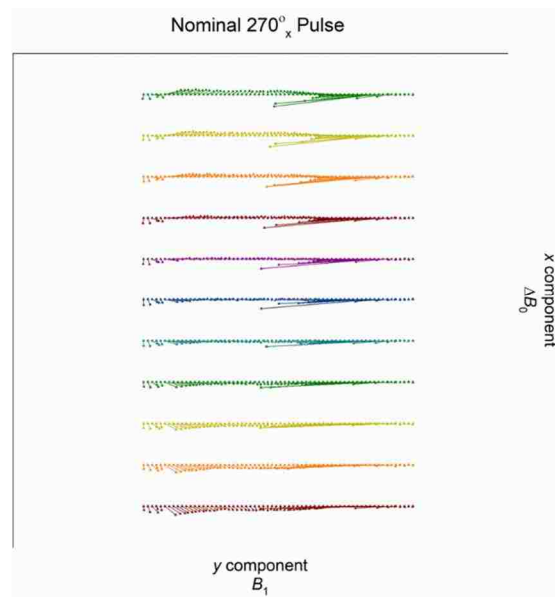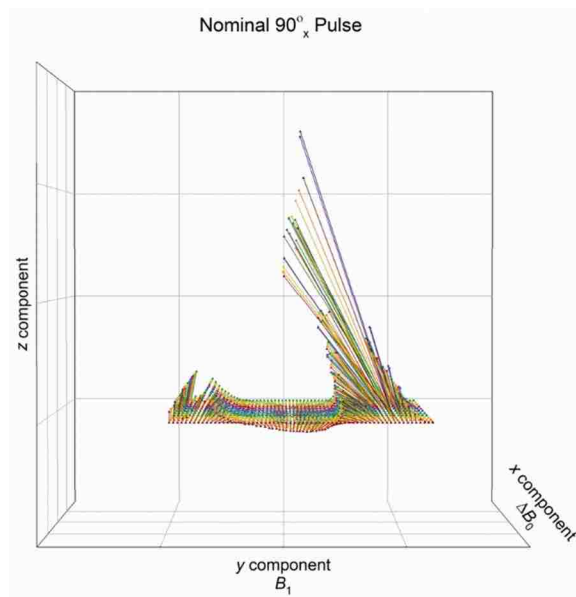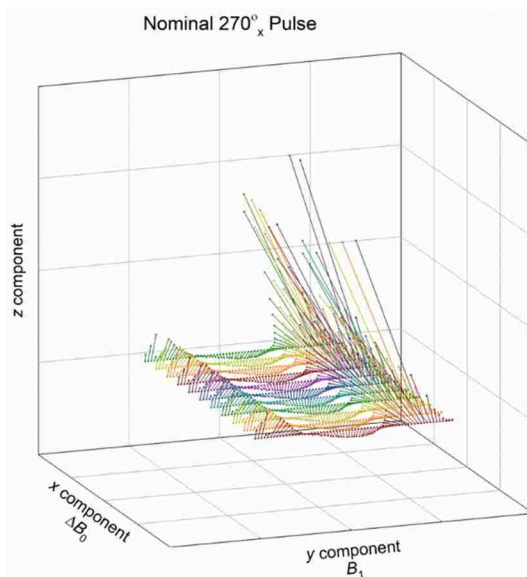
Pulse sequence for y nutation imaging with RIPT after a single pulse (zz_ript_y_1D)

```
define pulse px;
define loopcounter tdov;

"px=1u"                          ; dwell-pulse, "pulse" for receiving one data point
"tdov=td"                        ; loop increment for RIPT sequence
"d11=30ms"

      100u pl1:f1                ; set power level for F1, receiver
1     ze

start, d1 reset:f2 reset:f1      ; F1 and F2 initialization

      de1 fq=cnst1:f2 fq=cnst1:f1   ; set resonance offset for monitored pulse
      de1 pl3:f2                 ; set power level for F2, transmitter, monitored pulse
      (p3 ph3):f2                ; monitored pulse (or replace w/ a portion or entire sequence)

      de1 fq=0:f2 fq=0:f1        ; on resonance
      de2 adc ph31 syrec pl2:f2  ; open receiver and start digitizer
      de ph30:r

ifg,  d3                         ; nutation image (Interferogramm)
      px:x                       ; receive one data point
      3u:e
      (p1 ph1):f2 :e             ; RIPT pulse
lo to ifg times tdov

      10u
      rcyc=start
      d11 wr #0
exit

; ------- Phase program --------
ph3  = 0 0 2 2 1 1 3 3           ; phase for monitored pulse
ph2  = 0 2 3 1                   ; phase for EXCEPT monitored pulse
ph1  = 0 2 2 0 1 3 3 1           ; phase for RIPT pulse
ph30 = 0 0 2 2 1 1 3 3           ; receiver phase
ph31 = 0

                                 ;d1 : relaxation delay (z.B. 5xT1)
                                 ;d3 : delay between RIPT pulses
                                 ;p1 : RIPT pulse length (dpw)
                                 ;p2 : monitored pulse length
                                 ;td1: number of interferrograms (set in eda)
                                 ;TD : number of data points in the interferrogram
                                 ;NS : number of scans (ns = 2*n)
                                 ;cnst1 : resonance offset for monitored pulse
```

Pulse sequence for *z* nutation imaging with RIPT after a single pulse (zz_ript_z_1D)

```
define pulse px;
define loopcounter tdov;

"px=1u"                          ; dwell-pulse, "pulse" for receiving one data point
"tdov=td"                        ; loop increment for RIPT sequence
"d11=30ms"

      100u pl1:f1                 ; set power level for F1, receiver
1     ze

start, d1 reset:f2 reset:f1      ; F1 and F2 initialization

      de1 fq=cnst1:f2 fq=cnst1:f1 ; set resonance offset for monitored pulse
      de1 pl3:f2                 ; set power level for F2, transmitter, monitored pulse
      (p3 ph3):f2                ; monitored pulse (or replace w/ a portion or entire sequence)

      de1 fq=0:f2 fq=0:f1        ; on resonance
      de2 adc ph31 syrec pl2:f2  ; open receiver and start digitizer
      de ph30:r

ifg,  d3                         ; nutation image (Interferogramm)
      px:x                       ; receive one data point
      3u:e
      (p1 ph1):f2 :e             ; RIPT pulse
lo to ifg times tdov

      10u
      rcyc=start
      d11 wr #0
exit

; ------- Phase program --------
ph3 = 0 0 2 2 1 1 3 3            ; phase for monitored pulse
ph2 = 0 2 3 1                    ; phase for EXCEPT monitored pulse
ph1 = 0 2 2 0 1 3 3 1            ; phase for RIPT pulse
ph30 = 0 2 2 0 1 3 3 1           ; receiver phase
ph31 = 0

                                 ;d1 : relaxation delay (z.B. 5xT1)
                                 ;d3 : delay between RIPT pulses
                                 ;p1 : RIPT pulse length (dpw)
                                 ;p2 : monitored pulse length
                                 ;td1: number of interferrograms (set in eda)
                                 ;TD : number of data points in the interferrogram
                                 ;NS : number of scans (ns = 2*n)
                                 ;cnst1 : resonance offset for monitored pulse
```

BIBLIOGRAPHY

[1]   Friebolin, Horst. *Basic One- and Two-Dimensional NMR Spectroscopy*; New York, NY: Wiley-VCH, 2005.

[2]   Harris, Robin K.. "Nuclear Spin Properties & Notation." *Encyclopedia of Nuclear Magnetic Resonance*; Ed. David M. Grant, Robin K. Harris. New York: John Wiley, 2002.

[3]   Gerstein, B.C. "Rudimentary NMR: The Classical Picture." *Encyclopedia of Nuclear Magnetic Resonance*; Ed. David M. Grant, Robin K. Harris. New York: John Wiley, 2002.

[4]   Levitt, Malcolm H. *Spin Dynamics*; Chicester: Wiley-Blackwell, 2001.

[5]   Keeler, J. Chapter 13: How the Spectrometer Works. *Understanding NMR Spectroscopy*, 2nd Edition; Wiley, 2010; 483-494.

[6]   Hill, H.D.W. "Spectrometers: A General Overview." *Encyclopedia of Nuclear Magnetic Resonance*, Ed. David M. Grant, Robin K. Harris. New York: John Wiley, 2002.

[7]   Fukushima, E.; Roeder, S.B.W. *Experimental Pulse NMR: A Nuts and Bolts Approach*; Westview Press, 1993.

[8]   Nyquist, H. Certain Topics in Telegraph Transmission Theory. *Transactions A.I.E.E.* **1928**, 617-644.

[9]   Shannon, C.E. Communication in the Presence of Noise. *Proceedings of the IRE* **1949**, *37*, 10-21. DOI: 10.1109/JRPROC.1949.232969.

[10]   Bain, A.D. "Radiofrequency Pulses: Response of Nuclear Spins." *Encyclopedia of Nuclear Magnetic Resonance*; Ed. David M. Grant, Robin K. Harris. New York: John Wiley, 2002.

[11]   Howarth, O.W. "Recording One-Dimensional High Resolution Specra." *Encyclopedia of Nuclear Magnetic Resonance*; Ed. David M. Grant, Robin K. Harris. New York: John Wiley, 2002.

[12]   *Applications of NMR Spectroscopy*, Volume 1; Atta-ur-Rahman, M.; Choudhary, M.I.; Eds.; Bentham Science Publishers, 2015.

[13]   Gunther, H. *NMR Spectroscopy: Basic Principles, Concepts and Applications*; Wiley, 2013.

[14]   Kay, L.E. The Evolution of Solution State NMR Pulse Sequences Through the 'Eyes' of Triple-Resonance Spectroscopy. *Journal of Magnetic Resoance* **2019**, *306*, 48-54. DOI: 10.1016/j.jmr.2019.07.035.

[15]   Teodor, P. Towards Perfect NMR: Spin-Echo Versus Perfect-Echo Building Blocks. *Magnetic Resonance Chemistry* **2019**, *57*, 13-29. DOI: 10.1002/mrc.4776.

[16]   Stefan, B. A Quarter of a Cenury of SERF: The Progress of an NMR Pulse Sequence and its Application. *Progress in Nuclear Magnetic Resonance Spectroscopy* **2018**, *108*, 74-114. DOI: 10.1016/j.pnmrs.2018.10.001.

[17]   Hoult, D.I.; Richards, R.E. *Critical factors in the design of sensitive high resolution nuclear magnetic resonance spectrometers*. *Proc. Royal Soc. A*. **1975**, *334*, 311–340.

[18]   Becker, E.D. Chapter 3 Instrumentation and Techniques, 3.5 Phase Cycling. *High Resolution NMR - Theory and Chemical Applications*,3rd Edition,; Academic Press, 2000; pp. 49-82.

[19]   Levitt, M.H. Composite Pulses. *eMagRes* **2007**. DOI: 10.1002/9780470034590.emrstm0086.

[20]   Keeler, J.; Clowes, R.T.; Davis, A.L.; Laue, E.D. *Pulsed-field gradients: Theory and practice, Methods in Enzymology*, Volume 239, 1994, Pages 145-207.

[21]   Pfaff, A.R.; Woelk, K. A Fast and Convenient Way to Predict Relaxation during a Frequency-selective Adiabatic Hyperbolic Secant Pulse (HS1 Sech Pulse). *Applied Magnetic Resonance* **2018**, *49*, 479-491. DOI: 10.1007/s00723-018-0989-y.

[22]   Pfaff, A.R.; McKee, C.; Woelk, K. Predicting the Effect of Relaxation during Frequency-selective Adiabatic Pulses. *Journal of Magnetic Resonance* **2017**, *284*, 99-103. DOI: 10.1016/j.jmr.2017.09.014.

[23]   Metz, K.R.; Boehmer, J.P.; Bowers, J.L.; Moore, J.R. Rapid Rotating-Frame Imaging Using an RF Pulse Train (RIPT). *Journal of Magnetic Resonance, Series B* **1994**, *103*, 152-161. DOI: 10.1006/jmrb.1994.1023.

[24]   Hoult, D.I. Rotating Frame Zeugmatography. *Journal of Magnetic Resonance* **1979**, *33*, 183-197. DOI: 10.1016/0022-2364(79)90202-6.

[25]   Trautner, P.;Woelk, K. Fast Chemical-Shift T_1 Imaging in Toroid Cavities for the Structural Analysis of Gels and Emulsions. *Applied Magnetic Resonance* **2002**, *22*, 291-305.

[26]   Maffei, P.; Mutzenhardt, P.; Retournard, B. ; Diter, B.; Raulet, R.; Brondeau, J.; Canet, D. NMR Microscopy by Radiofrequency Field Gradients. *Journal of Magnetic Resonance, Series B* **1994**, *107*, 40-49.

[27]   Doty, David. "Probe Design and Construction." *Encyclopedia of Nuclear Magnetic Resonance*; Ed. David M. Grant, Robin K. Harris. New York: John Wiley, 2007.

[28]   Bakhmutov, Vladimir I. *Practical NMR Relaxation for Chemists*; Hoboken, NJ: Wiley, 2002.

[29]   Traficante, D.D. "Relaxation: An Introduction." *Encyclopedia of Nuclear Magnetic Resonance*, Ed. David M. Grant, Robin K. Harris. New York: John Wiley, 2002.

[30]   Morgan, L.O.; Nolle, A.W. Proton spin relaxation in aqueous solutions of paramagnetic ions. II. Cr^{+++}, Mn^{++}, Ni^{++}, Cu^{++}, and Gd^{+++}. *Journal of Chemical Physics* **1959**, *31*, 365-368. DOI: 10.1063/1.1730360.

[31]   Satterfield, E.T.; Pfaff, A.R.; Zhang, W.; Chi, L.; Gerald, R.E.II.; Woelk, K. EXponentially Converging Eradication Pulse Train (EXCEPT) for solvent-signal suppression in investigations with variable T_1 times. *Journal of Magnetic Resonance* **2016**, *268*, 68-72. DOI: 10.1016/j.jmr.2016.05.005.

[32]   Silver, M.S.; Joseph, R.I.; Hoult, D.I. Highly selective and π pulse generation. *Journal of Magnetic Resonance* **1984**, *59*, 2, 347-351. DOI: 10.1016/0022-2364(84)90181-1.

[33]   Tannus, A.; Garwood, M. Adiabatic pulses. *NMR in Biomedicine* **1997**, *10*, 8, 423-434. DOI: 10.1002/(sici)1099-1492(199712)10:8<423::aid-nbm488>3.0.co;2-x.

[34]   Zhang, S.; Yang, X.; Gorenstein, D. G. Enhanced Suppression of Residual Water in a "270" WET Sequence. *Journal of Magnetic Resonance* **2000**, *143*, 382-386. DOI: 10.1006/jmre.1999.1987.

VITA

Emmalou Theresa Schmittzehe was born in Kansas City, Missouri on August 5, 1982. In August 2000 she began her undergraduate studies and in May 2005 she received her B.S. degree in Chemistry from the University of Missouri-Rolla (now Missouri University of Science and Technology). In August 2005 Emma entered graduate school performed research in the field of NMR under the direction of Dr. Klaus Woelk. She received her M.S. degree in Chemistry in December 2011 from Missouri University of Science and Technology. Emma continued graduate school part time as she also taught as an Assistant Teaching Professor at Missouri University of Science and Technology. During that time, she implemented a complete redesign of the first-semester general chemistry course providing students with different learning options and emphasizing active learning to improve student success. In December 2019 She received her PhD in Chemistry from Missouri University of Science and Technology.